Climatology of Cirrus Clouds over Observatory of Haute-Provence (France) Using Multivariate Analyses on Lidar Profiles

Florian Mandija, Philippe Keckhut, Dunya Alraddawi, Sergey Khaykin, Alain Sarkissian

atmosphere

MDPI

Article

Climatology of Cirrus Clouds over Observatory of Haute-Provence (France) Using Multivariate Analyses on Lidar Profiles

Florian Mandija *, Philippe Keckhut, Dunya Alraddawi, Sergey Khaykin and Alain Sarkissian

Laboratoire Atmosphères, Observations Spatiales (LATMOS), Institut Pierre-Simon Laplace (IPSL), Université de Versailles-Saint-Quentin-en-Yvelines (UVSQ)/Paris-Saclay University, Sorbonne University, Centre National de la Recherche Scientifique (CNRS), 78280 Guyancourt, France; philippe.keckhut@latmos.ipsl.fr (P.K.); dunya.alraddawi@latmos.ipsl.fr (D.A.); sergey.khaykin@latmos.ipsl.fr (S.K.); alain.sarkissian@latmos.ipsl.fr (A.S.)
* Correspondence: florian.mandija@latmos.ipsl.fr; Tel.: +33-605556870

Abstract: This study aims to achieve the classification of the cirrus clouds over the Observatory of Haute-Provence (OHP) in France. Rayleigh–Mie–Raman lidar measurements, in conjunction with the ERA5 dataset, are analyzed to provide geometrical morphology and optical cirrus properties over the site. The method of cirrus cloud climatology presented here is based on a threefold classification scheme based on the cirrus geometrical and optical properties and their formation history. Principal component analysis (PCA) and subsequent clustering provide four morphological cirrus classes, three optical groups, and two origin-related categories. Cirrus clouds occur approximately 37% of the time, with most being single-layered (66.7%). The mean cloud optical depth (COD) is 0.39 ± 0.46, and the mean heights range around 10.8 ± 1.35 km. Thicker tropospheric cirrus are observed under higher temperature and humidity conditions than cirrus observed in the vicinity of the tropopause level. Monthly cirrus occurrences fluctuate irregularly, whereas seasonal patterns peak in spring. Concerning the mechanism of the formation, it is found that the majority of cirrus clouds are of in situ origin. The liquid-origin cirrus category consists nearly entirely of thick cirrus. Overall results suggest that in situ origin thin cirrus, located in the upper tropospheric and tropopause regions, have the most noteworthy occurrence over the site.

Keywords: cirrus clouds; climatology; classification; lidar measurements; ERA5 database

Citation: Mandija, F.; Keckhut, P.; Alraddawi, D.; Khaykin, S.; Sarkissian, A. Climatology of Cirrus Clouds over Observatory of Haute-Provence (France) Using Multivariate Analyses on Lidar Profiles. *Atmosphere* **2024**, *15*, 1261. https://doi.org/10.3390/atmos15101261

Academic Editor: Mario Marcello Miglietta

Received: 14 August 2024
Revised: 15 October 2024
Accepted: 16 October 2024
Published: 21 October 2024

1. Introduction

According to the International Cloud Atlas of the World Meteorological Organization (WMO), clouds are classified into ten basic types, which are further divided into three major categories; high-level, mid-level, and low-level clouds (https://cloudatlas.wmo.int/en/cloud-classification-summary.html, accessed on 18 November 2024). High-level clouds, in turn, are subdivided into three types: cirrus, cirrostratus, and cirrocumulus [1].

Cirrus clouds are associated with synoptic scale motions, such as orographic uplift in the upper troposphere, frontal uplift, convective systems, and large-scale raising [2–9]. In European mid-latitude regions, the prevalent cirrus clouds come through slow updrafts in frontal systems, such as warm conveyor belts, and other dynamic phenomena like jet streams, mountain waves, and convection [10]. These contain both liquid-origin and in situ origin cirrus [11]. Cirrus clouds are predominantly or entirely composed of non-spherical ice crystals with a variety of shapes [12]. For the most part, cirrus clouds have a net warming effect, even though this varies depending on their characteristics.

Concerning optical depth, there are three categories of ice clouds: subvisible (SVS), visible, and opaque clouds [13,14]. Numerous efforts have been made to identify additional classes of cirrus clouds. Thus, a clustering classification technique was used by [15], where up to six classes of clouds were identified based on their optical depth, ranging from thick clouds to very thin clouds, with three classes corresponding to cirrus clouds, which is also the focus of this paper.

Regarding their formation mechanism, cirrus clouds have been classified as liquid and in situ origin [16–18]. In situ origin cirrus are formed directly from water vapor at T < −38 °C, RH_{ice} > 100%, and RH_w < 100%, and liquid-origin cirrus evolve from the freezing of liquid drops in clouds at T $\gtrsim$ −38 °C and RH_w~100%. In situ origin cirrus are thinner, located at the altitudes where they are formed, whereas liquid-origin cirrus are thicker and uplifted from lower altitudes [9,10,18,19]. Cirrus clouds that originate from liquids are typically associated with frontal systems (or convection). In contrast, cirrus clouds that form in situ are connected to jet streams, mountain waves, and high-pressure systems [10,20]. In situ cirrus have a lower optical depth (up to 1.0), producing a slight net warming effect (up to 10 $W \cdot m^{-2}$), while liquid-origin cirrus have a higher optical depth (1.0 to 3.0), and a strong net cooling effect (−15 to −250 $W \cdot m^{-2}$) [17].

Lidar high-resolution measurements of the vertical distribution of clouds provide unique information that is not obtained with passive instruments for developing a highly detailed climatology of cirrus cloud variability [21–30]. Lidar vertical-resolved cloud profiles are used in combination with the meteorological parameters provided by nearby radiosondes or datasets of the ERA5 to provide more insights about the cloud properties and thermodynamical conditions.

Numerous studies on cirrus clouds in mid-latitude regions have been conducted [10,13,31–51]. The main findings concerning cirrus occurrence properties reported by several authors are summarized in Table 1. The majority of studies indicate that cirrus clouds at mid-latitudes are formed at altitudes of 9 to 10 km, with very large variability of the geometrical and optical depths. Their mid-cloud temperatures (T) usually range in the interval of −50 to −60 °C. Usually, a slightly smaller percentage of the subvisible and a higher percentage of the visible clouds were observed. In addition, no set percentages of optical groups were observed in the mid-latitude regions. Nevertheless, no systematic differences were noted between the mid-latitude results and those of other regions.

Table 1. Summarized are the general cirrus results (cloud mean height—CMH, geometrical depth—CGT, optical depth—COD, mid-cloud temperature—T) and the occurrences reported in previous studies. Occurrences are presented as percentages of the total cirrus occurrences, and categorized as subvisible, visible, and opaque. Criteria for CMH and T, along with the selected lidar ratio (LR) used in various studies for cirrus identification, are also presented here.

Previous Results					Criteria			Ref.
CMH (km)	**CGT (km)**	**COD**	**T (°C)**	**Occurr. (%)**	**CMH (km)**	**T (°C)**	**LR (sr)**	
Mid-latitude regions								
10.3 ± 0.9	2.7 ± 0.9	0.31 ± 0.24	−51 ± 5.5	53 (3-57-40)	8	−38	25	[31]
7.8 ÷ 11.2	1.2 ÷ 4.3	0.37 ± 0.18	−58 ÷ −36	30 (10-49-41)	–	–	31	[32]
–	–	0.14 ± 0.13	–	30 (36-50-14)	–	−38	–	[33]
10.3 ± 1.2	1.8 ± 1.1	0.36 ± 0.45	−51 ± 8.0	26 (14-48-38)	7	−37	–	[36]
10.0 ± 1.3	1.4 ± 1.3	–	–	39 (20-23-57)	–	−25	18	[37]
9.0 ÷ 10.0	2.1 ÷ 2.4	1.18 ÷ 1.23	−50 ÷ −45	–	–	−37	25	[38]
9.2 ± 1.9	1.6	0.36	–	–	5	−40	–	[39]
9.7 ± 1.6	1.6 ± 1.5	–	−50 ± 9.5	–	7	−25	25	[51]
10.1 ± 1.7	1.6 ± 1.1	0.07 ÷ 0.50	−52 ÷ −38	37 (38-32-30)	–	−25	–	[41]
8.6 ÷ 11.5	0.9 ÷ 3.2	0.13 ÷ 0.80	−58 ÷ −41	47 (23-50-27)	–	–	18	[43]
Other regions								
9.8 ± 1.7	1.5 ± 0.7	0.45 ± 0.30	−39 ± 5.0	11 (0-80-20)	6	−27	27	[47]
10.0 ± 0.8	1.6 ± 0.7	0.30 ± 0.30	−40 ± 6.0	64 (2-61-37)	6	−27	27	[47]
12.8 ± 1.5	1.8 ± 1.0	0.28 ± 0.29	−58 ± 11	43 (8-52-40)	9	–	30	[52]
13.6 ± 2.1	1.4 ± 1.1	0.25 ± 0.46	–	74 (42-38-20)	–	−37	23	[48]
14.7 ± 1.8	1.7	0.33 ± 0.29	−65 ± 12	15 (16-34-50)	9	−40	28	[49]
–	–	0.37± 0.25	–	–	8	−20	27	[53]
10.1	3.0 ± 0.9	0.26 ± 0.11	−65 ± 4.0	(0-68-32)	8	–	32	[50]

This study aims to synergically classify cirrus clouds according to their morphology, optical properties, and formation mechanism. The paper is organized as follows: Section 2 presents the instrumentation, the characteristics of the datasets used, and the methodology used to evaluate the cirrus properties. Section 3 gives the results of the multivariate analysis of the cirrus properties, performing a threefold cloud classification. Section 4 summarizes the main results.

2. Materials and Methods

2.1. Lidar Description

In climatological investigations, lidar instrumentation plays a crucial role, particularly when studying thin or very thin cirrus clouds. Multiple lidar stations have been employed in systematic climatological investigations of cirrus clouds within the mid-latitudes. Some of them are located at European sites, such as Haute-Provence and Clermont-Ferrand in France, Jülich in Germany, Zürich and Jungfraujoch in Switzerland, Rome Tor Vergata in Italy, etc. [2,32,33,36,41].

Originally designed for Rayleigh scattering to derive temperature and study stratospheric aerosols, the lidar used in this study was enhanced in 1994 with additional channels for water vapor, nitrogen density, and aerosols, facilitating simultaneous cirrus retrieval. The Rayleigh–Mie–Raman lidar, stationed at the Observatory of Haute-Provence (the site is located at 43.9° N, 5.7° E, and 679 m altitude), conducts year-round night-time measurements, except during low cloud cover. It typically operates for about 6 h per session, with varying duration based on factors like cloud cover and operator availability [42,43,54]. This lidar employs a doubled Nd-YAG laser emitting a light pulse of approximately 10 nanoseconds at 532 nm, with a repetition rate of 50 Hz and an average pulse energy of 300 mJ. Backscattered photons are collected using optical fibers. The Nitrogen Raman channel, an upgrade of the Rayleigh temperature lidar within the Network for the Detection of Atmospheric Composition Change (NDACC), utilizes a 20 cm telescope and a 1 mm diameter optical fiber [55]. The field of view is 1 mrad. The cirrus detection system consists of a primary lens, an interference filter, and a mechanical electric shutter system that minimizes noise from the initial burst. Adjusting photon flux optimizes signal quality and retrieval accuracy. To mitigate specular reflections, the lidar beam is angled away from the zenith by a few degrees. Lidar observations have a temporal resolution of 160 s and a vertical resolution of 75 m, which is satisfactory for identifying different layers and small-scale cirrus.

2.2. Cloud Retrievals

During the period between 2021 and 2023, the lidar system collected more than 4000 h of measurements, providing a profile for each 160 s. Here, the vertical profile of the lidar backscattering ratio (BSR) was used to measure the scattering intensity and the cloud geometrical depth; both were used to determine the cloud optical depth. This parameter is related to the particle scattering efficiency and particle number density.

The process of retrieving cirrus optical depth using a lidar involves making certain assumptions. The cloud optical depth was obtained from BSR profiles by the following expression given by [37]. So, the cloud optical depth (COD) at a certain altitude z_o is given by integrating the total volume scattering coefficient $\beta(z)$.

$$COD(\lambda, z_o) = \int_{zo}^{\infty} \beta(\lambda, z) dz \quad (1)$$

On the other hand, the total volume scattering coefficient $\beta(z)$ is given as the product of the total scattering cross section per molecule $\sigma(z)$ and the molecular number density $N(z)$.

$$\beta_{Rayleigh}(\lambda, z) = n_{air}(z) \cdot \sigma_{Rayleigh}(z) \quad (2)$$

$$\tau(\lambda, z_o) = \eta \cdot (LR)\sigma_{Rayleigh} \int_{zmin}^{zmax} n_{air}(z)[SR(z) - 1]dz \quad (3)$$

$$\tau(\lambda, z_o) = \eta \cdot (LR)\sigma_{Rayleigh} \int_{zmin}^{zmax} n_{air}(z)BSR(z)dz \quad (4)$$

Tabular values of each volume scattering coefficient b(z) and the total scattering cross section at several wavelengths, 0.20–0.90 mm, have been provided by [56].

The lidar scattering ratio was obtained from the Mie (aerosol) and Rayleigh (molecular) scattering coefficients, and it is usually defined as the ratio of the cirrus backscattering (excluding background aerosol contribution) to the total backscattering:

$$SR = \frac{\boldsymbol{\beta_{aerosol}(\lambda, z) + \beta_{Rayleigh}(\lambda, z)}}{\boldsymbol{\beta_{Rayleigh}(\lambda, z)}} \quad (5)$$

In free-sky conditions, SR is equal to unity. In our case, the wavelength was 532 nm. In this case, $\sigma(z) = 5.245$ cm^2 and $\beta(z) = 1.336$ km^{-1}.

Mid-cloud height (CMH) was determined using the lidar scattering ratio.

$$\boldsymbol{CMH} = \frac{\int_{z_{base}}^{z_{top}} \boldsymbol{z' \cdot SR(z') \cdot dz'}}{\int_{z_{base}}^{z_{top}} \boldsymbol{SR(z') \cdot dz'}} \quad (6)$$

To construct the cirrus cloud database, a methodology similar to [57] was employed, adjusting integration times based on discontinuities in the optical depth time series. An iterative approach, motivated by [58], was adopted to identify multiple change points within the value series.

Although there is no widely accepted criterion for identifying cirrus clouds, they are discerned based on two criteria: a temperature threshold and a scattering ratio above a defined threshold [59]. The temperature threshold and the cloud altitude range, even though comparable, are not uniform throughout the previous studies (Table 1). Numerous investigations on cirrus clouds have utilized temperature thresholds ranging from −25 °C to −38 °C [12,27,60,61]. A temperature threshold of −38 °C, where ice can nucleate homogeneously without the presence of ice-nucleating particles (INPs), was used here [62]. Regarding the cirrus mean altitude, a diapason ranging from 6 to 9 km was applied by [53,60,63], etc. To estimate the cirrus cloud boundaries, an SR threshold was defined as the average plus three times its standard deviation of the background, in this case, 17–19 km, altitude range [41,43]. Cirrus clouds distant by less than 500 m from each other were considered as one cirrus cloud layer [31]. Only clouds with a vertical extension above 150 m were taken into account [33,60].

The value of the lidar ratio dominates the errors associated with the optical depth determination [64]. For consistent analysis, a constant lidar ratio of 25 sr was used across different cloud types, which was also the case in this study [51,53]. Nevertheless, other papers recommended different values of lidar ratio [36,65,66] (Table 1). The lidar ratio increases with the cloud thickness, and it is influenced by multiple scattering effects [47]. In addition, a value of η = 0.75 was chosen, introducing an approximate 20% uncertainty into the retrieved optical depth [51].

2.3. Meteorological Retrievals

Because cirrus clouds are a product of weather processes that inject water vapor into the dry upper troposphere, which are a strong function of latitude (the redistribution of the solar heating) and longitude (due to the circulation features), their properties depend strongly on the measurement location.

The ERA5 represents the fifth generation of the European Center for Medium-Range Weather Forecasts—ECMWF. The ERA5 reanalysis provides meteorological data, such as

air temperature, relative humidity, cloud ice water content, atmospheric pressure, vertical velocity, etc., which are then used to expound on the synoptic features.

Gridded data provided by the ERA5 have a horizontal resolution of 0.25° × 0.25°. It provides vertical coverage between 1000 hPa to 1 hPa, with a vertical resolution of 37 pressure levels, and hourly temporal resolution [67]. Because the nearest local meteorological measurements were carried out by radio soundings in Nimes, which is about 100 km away from the OHP, the ERA5 reanalysis dataset was preferable for these analyses.

2.4. Cloud Classifications

Multifold cirrus classification is essential to categorize these clouds from various perspectives. This process was undertaken in three consecutive phases:

Cirrus Classes based on the cloud morphology;

Cirrus Groups based on the optical properties;

Cirrus Categories based on their formation mechanism.

Primarily, a principal component analysis was performed to provide inputs for clustering. Concerning cloud property data such as the temperature, relative humidity, ice water content, altitude, etc., several methods could provide inputs for clustering, such as principal component analysis (PCA), Factor Analysis (FA), Non-negative Matrix Factorization (NMF), T-distributed Stochastic Neighbor Embedding (t-SNE), Autoencoders, Multidimensional Scaling (MDS), Correspondence Analysis (CA), etc. Given the nature of cirrus data (continuous and correlated cloud properties), PCA or FA are good starting points for dimensionality reduction. Because of significative linear correlations expected between mid-height altitude and temperature on one hand, and cloud geometrical and optical depth on the other, the PCA method was preferred to FA. PCA is a statistical technique used to simplify a dataset by reducing its dimensionality, which can make data analysis more tractable. Among various statistical methods, PCA is extensively utilized in atmospheric sciences [43,68,69]. A key advantage of PCA is its ability to reproduce nearly all the variability in a dataset with high accuracy by using only a few principal components (PCs).

Here, eight original variables, such as the base-, mid-, and top-cloud altitudes, mid-cloud temperature, cloud geometrical and optical depths, relative humidity, and cloud ice water content, were transformed into only two meaningful PCs, relating to cloud altitude and depth. The Kaiser criterion determined the number of PCAs, which retained only the most important PCs, whose eigenvalues were greater than 1.

Clustering methods such as the k-means and Partitioning Around Medoids (PAM) methods are commonly used for partitioning clouds into different groups [43,70,71]. K-means clustering divides data into k clusters by minimizing squared distances between points and their centroids, iteratively updating centroids based on the mean of assigned points. Meanwhile, PAM clustering selects representative objects called "medoids" and assigns each point to the nearest medoid, minimizing dissimilarity within clusters. Here, both methods were applied to partition the dataset into four distinct and non-overlapping clusters, characterized by different cloud properties, here called cirrus classes. The determination of the optimal number of clusters was performed automatically by combining the silhouette, gap statistic, and elbow methods [72]. The silhouette method identifies the optimal number of clusters by maximizing the average silhouette score, indicating well-separated clusters. The gap statistic compares clustering performance to a random reference, with the optimal clusters where the gap is largest. The elbow method finds the point where adding more clusters yields diminishing returns in reducing within-cluster variation, forming an "elbow" on the plot.

The second cirrus classification provided three cirrus groups: subvisible (0.03 > COD), thin (0.03 < COD < 0.3), and thick or opaque (COD > 0.3) [73].

In the meantime, cirrus clouds were divided into two categories based on their production mechanism: liquid origin and slow/fast in situ origin.

This task was undertaken with regard to the two criteria: optical depth (COD) and ice water content (CIWC) [11,26]. COD thresholds between the three categories were 0.05 and 1.0, using an overall limit of 3.0 to exclude aerosol plumes, which are frequent in these latitudes [74,75]. Meanwhile, the threshold of CIWC between in situ and liquid-origin cirrus was 10^{-6} kg·m^{-3}.

3. Results

3.1. Occurrence and Statistical Characteristics of Cirrus Clouds

During the period of January 2021–August 2023, 356 days were analyzed, of which about 43.3% (154 days) were characterized by cirrus clouds. A similar result was obtained by [41], who detected cirrus during 37% of the total observation time, and by [37] on the OHP, who reported 54% cirrus occurrence and 25% of occurrences being subvisible. These differences arose because of the different definitions of cirrus occurrence.

Of these cirrus cases, single-layer structures were present in 66.7% of cases, while multi-layer structures were present in 33.3% of cases. A higher single-layer percentage of 80–20% is reported by [40], and even higher, 89–11%, by [13]. In the case of a double-layer structure, the mean cloud geometrical depth was reduced by 12%. This result was from a previous study [40], which suggested a CGT reduction of 10% in the case of a double-layer structure.

The mean values of the cloud properties of mean height, geometrical depth, and mid-cloud temperature are 10.8, 1.6 km, and −54.9 °C. Comparable results for CMH and CGT, but lower mid-cloud temperature, have been reported by [13,31,36–38,41]. The mean cloud optical depth found in this study was 0.39 ± 0.46. This result is comparable with the other results in mid-latitude regions (0.31 ÷ 0.37) [31,32,36,38]. As in previous investigations [12,14,31,76], CGT and COD were linearly fitted by the determination coefficient of R^2 = 0.57 (Figure 1a).

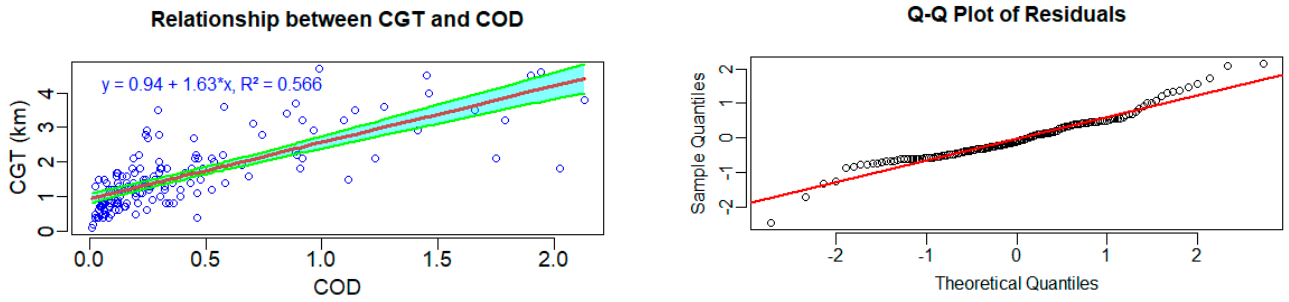

(**a**) (**b**)

Figure 1. (**a**) Scatterplot of cloud geometric and optical depths, using a confidence interval of level 0.95 (green space). Associated with a regression line, which fits a linear model (red line). (**b**) Q-Q plot which checks the normality of residuals. Red line represents the reference line, while black circles are the residuals.

In addition, the linear relationship was also statistically significant ($p < 0.05$). The mean of the residuals is very close to zero, which indicates no systematic bias. The Q-Q plot was used to visually confirm the normality distribution of the residuals (Figure 1b). CGT is significantly correlated with COD, by a coefficient of 0.75. Meanwhile, a very low correlation was obtained in the case of the dependencies of CGT and COD on T and CIWC. A low correlation between COD and CIWC was also obtained. The maximum of these correlations was obtained in the interval −65–45 °C, at slightly higher temperatures compared to the tropical regions [77], giving rise to the conclusion that mid-latitude cirrus are usually thicker and warmer than tropical cirrus.

3.2. Cirrus Clustering

The very first step in the cirrus characterization and classification was the preliminary study of the probability density functions (PDFs) of the cloud characteristics, such as cloud base height (CBH), cloud mean height (CMH), cloud top height (CTH), cloud geometrical depth (CGT), cloud optical depth (COD), and mid-cloud temperature (T). PDFs for the above-mentioned cloud parameters are presented in Figure 2.

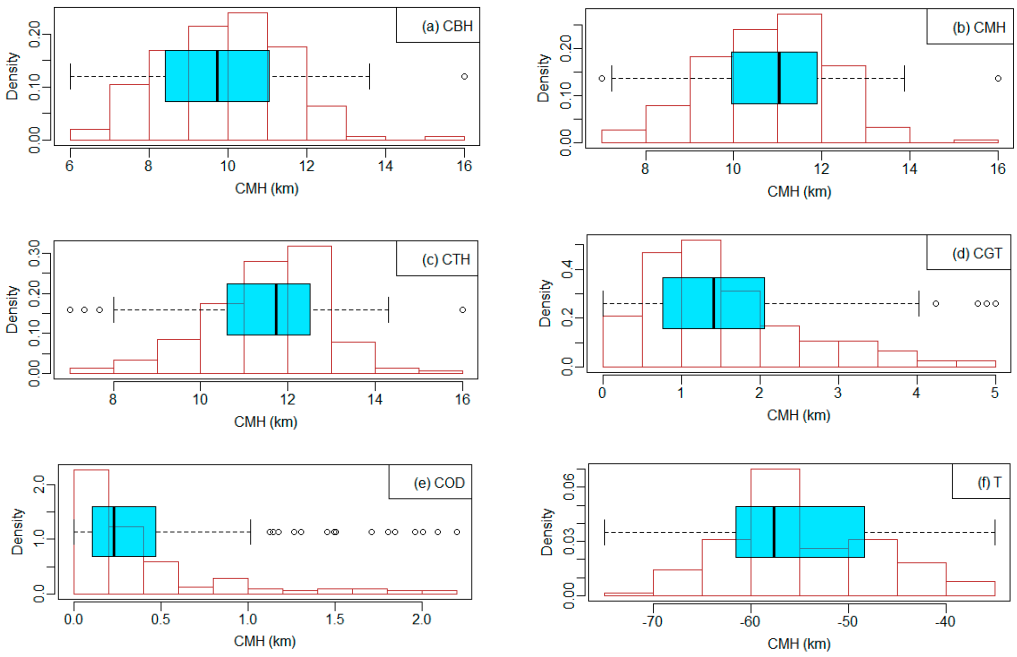

Figure 2. Histograms of PDFs for cloud base, mid, and top heights, cloud geometrical and optical heights, and mid-cloud temperature. Unimodal and bimodal distributions have been obtained. Blue box plots are included to present data distributions in a more summarized way.

The probability distribution functions revealed non-Gaussian multimode distributions, however, characterized by clear principal modes. Table 2 shows all the modes associated with the respective densities.

Table 2. Principal modes of the distributions of the values of cloud heights, cloud depths, and mid-cloud temperature. In addition, the associated densities of these modes are presented.

	CBH (km)	CMH (km)	CTH (km)	CGT (km)	COD	T (°C)
1st mode	10.5	11.3	12.2	1.26	0.12	−58.3
1st density	0.24	0.30	0.33	0.49	1.98	0.06
2nd mode	15.2	15.4	15.6	2.94	0.91	−49.2
2nd density	0.005	0.006	0.007	0.10	0. 25	0.03

Interestingly, the distribution of cloud heights shows only a unimodal pattern: CBH—10.5 km, CMH—11.3 km, and CTH—12.2 km. Conversely, the cloud depth distributions exhibit a bimodal structure: CGT—1.3 and 2.9 km, and COD—0.12 and 0.91. Temperature, in turn, shows one principal mode (−58.3) and a secondary one (−48.9 °C). Furthermore, additional modes of much lower density have been identified.

Temperature and cloud height clustering have been used to further classify the cirrus depending on their characteristics [7,41]. Four clusters were suggested by silhouette, elbow, and gap statistics methods [78]. The mean values of the cirrus properties in these clusters are shown in Table 3.

Table 3. Cirrus geometrical and optical properties: base-, mid-, and top-cloud height, temperature, geometrical and optical depth, as well as the frequency of occurrences for each cirrus class. Cirrus types based on their thickness and their locations in the atmosphere are given.

Class	CBH (km)	CMH (km)	CTH (km)	CGT (km)	COD	T (°C)	Type	Position	Occurr. (%)
K-means method (original data)									
1	11.2	11.7	12.3	1.18	0.23	−64.0	Thin	Tropopause	22.1
2	10.4	11.3	12.2	1.80	0.49	−57.2	Thick	Tropopause	43.5
3	9.3	10.0	10.8	1.58	0.37	−48.4	Moderate	Upper troposphere	23.4
4	7.8	8.6	9.3	1.52	0.37	−41.3	Moderate	Mid-troposphere	11.0
PAM method (original data)									
1	10.7	11.4	12.1	1.40	0.19	−61.3	Moderate	Tropopause	36.6
2	10.2	11.1	11.9	1.70	0.12	−55.6	Thick	Tropopause	30.7
3	9.0	9.8	10.5	1.50	0.24	−47.9	Moderate	Upper troposphere	22.9
4	8.5	8.8	9.0	0.50	0.07	−41.3	Thin	Mid-troposphere	9.8

Cirrus of class 1, found at the highest altitudes, are known as tropopause cirrus clouds. Their mid-cloud height is about 11.5 km. These cirrus clouds are geometrically the thinnest, 1.3 km. Tropopause thin cirrus clouds (similar to class 1) are associated with the large-scale transport processes of moist tropical and sub-tropical air masses named synoptic cirrus, having a relatively short duration, typically less than a day [48].

The thick cirrus of class 2 are situated at somewhat lower heights compared to the first one. This class is geometrically the thickest, 1.8 km. Thick low tropopause and/or upper tropospheric cirrus (similar to classes 2 and 3) probably come from standard meteorological phenomena and the large-scale fast ascension of warm air masses. The so-called upper tropospheric cirrus (class 3) are situated at lower altitudes, CMH 10 km, and have a moderate geometrical depth of 1.6 km. Both methods provide a similar frequency of occurrence in this class, around 23%.

Cirrus class 4 is the lowest one in terms of their geometrical heights, CMH 8.7 km. This cirrus class is less frequent, identified in only about 11% of the cases. Additionally, within the mid-tropospheric cirrus category (similar to class 4), the contribution of contrails can also be anticipated, leading to the formation of what is known as contrail cirrus. These clouds could be triggered by old and persistent contrails through the heterogenous nucleation incited by aircraft exhausts. Even though the majority of aircraft routes pass over upper tropospheric regions, there are not ideal conditions for cirrus development. However, the mid-tropospheric region over Europe is saturated with respect to ice, which favors the persistence of contrails and the formation of the contrail cirrus upon the fulfilment of the Schmidt–Appleman criterion [9,46,79–82].

3.3. Principal Component Analysis—PCA

The results of the two clustering methods applied to the original data showed significant discrepancies, necessitating the use of PCA, which produces more consistent findings. Moreover, PCA is used to minimize the dataset's dimensions and eliminate the highly associated variables. This method is also effectively used in other cirrus climatology investigations [32,43,83].

In this case, the cloud heights CBH, CMH, and CTH, but also the cloud mean temperature result, strongly interconnected. Under these conditions, the usage of a new variable which represented the qualities of these cloud properties was advantageous. To establish the optimal number of PCs that adequately explained the variance in the data, the Kaiser criterion was used [84,85].

The eigenvalues of Table 4 show that only the first two PCs account for 68.5% of the total variance. In Figure 3, the scree plot is used to visualize the quality of the representation

of the old variables on the new principal components [86]. A very similar result was provided by [32,41,43].

Table 4. Determination of the number of retained principal components. Eigenvalues corresponding to the amount of the variation explained by each PC. Only PCs with eigenvalues higher than 1 can be taken into account, in this case PC1 and PC2.

	Eigenvalue	Variance (%)	Cumulative Variance (%)
PC 1	3.6	44.4	44.4
PC 2	1.9	24.1	68.5
PC 3	1.0	13.1	81.6
PC 4	0.9	11.7	93.3
PC 5	0.3	3.5	96.7
PC 6	0.3	3.3	100
PC 7	3×10^{-31}	4×10^{-30}	100
PC 8	8×10^{-32}	1×10^{-30}	100

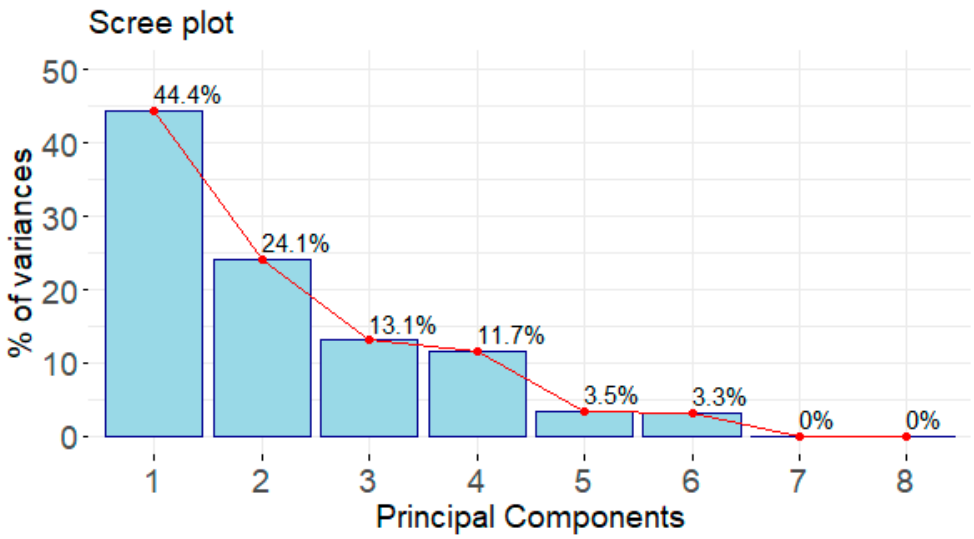

Figure 3. Scree plot used to visualize the contributions of PCs to the total variance. Every bar represents the contributions of each of the eight PCs. The cutoff is set at the first two PCs (68.5%).

The function Cos2 is widely used to determine the quality of the representation of a variable on a principal component. For a given variable Xi and a principal component PCj, the function of the Cos2 is calculated by the following equation:

$$\boldsymbol{Cos2}(\boldsymbol{X_i}, \boldsymbol{PC_j}) = \left(\frac{\boldsymbol{coordinate\ of\ X_i\ on\ PC_j}}{\sum_{k=1}^{m} (\boldsymbol{coordinate\ of\ X_i\ on\ PC_k})} \right)^2 \quad (7)$$

m is the total number of principal components.

PC values (Table 5) or Cos2 function (Figure 4) indicate that PC1 better represents cloud locations (CBH, CMH, CTH, and T), and PC2 better represents cloud thickness (CGT and COD). Furthermore, PC3 represents cloud microphysical properties (CIWC and less RH_w). With only 18% of the variation, the remaining PCs (PC4, PC5, PC6, PC7, and PC8) are far less significant.

Table 5. PC scores for all the cirrus parameters: CBH, CMH, CTH, CT, COD, T, RH, and CIWC. Higher PC values determine the importance of components for each of the cirrus parameters.

	PC1	PC2	PC3	PC4	PC5	PC6	PC7	PC8
Cloud base height (CBH)	0.52	−0.10	0.10	−0.05	−0.30	0.07	0.46	−0.64
Cloud mean height (CMH)	0.51	0.12	0.07	−0.10	−0.16	0.20	−0.80	−0.06
Cloud top height (CTH)	0.45	0.35	0.02	−0.14	0.02	0.33	0.39	0.63
Cloud geometrical depth (CGT)	−0.18	0.63	−0.13	−0.12	0.48	0.34	0.004	−0.44
Cloud optical depth (COD)	−0.16	0.61	−0.12	−0.14	−0.60	−0.45	2×10^{-16}	4×10^{-17}
Mid-cloud temperature (I)	−0.42	−0.19	−0.07	−0.39	−0.47	0.64	8×10^{-16}	7×10^{-16}
Relative humidity (RH)	−0.17	0.21	0.54	0.71	−0.22	0.28	3×10^{-16}	-1×10^{-16}
Cloud ice water content (CIWC)	−0.10	0.02	0.81	−0.53	0.14	−0.18	-6×10^{-17}	2×10^{-16}
Standard deviation	1.89	1.39	1.02	0.97	0.53	0.51	6×10^{-16}	3×10^{-16}
Proportion of variance	0.44	0.24	0.13	0.12	0.03	0.03	0×10^{0}	0.00
Cumulative Proportion	0.44	0.68	0.82	0.93	0.97	1.00	1.00	1.00

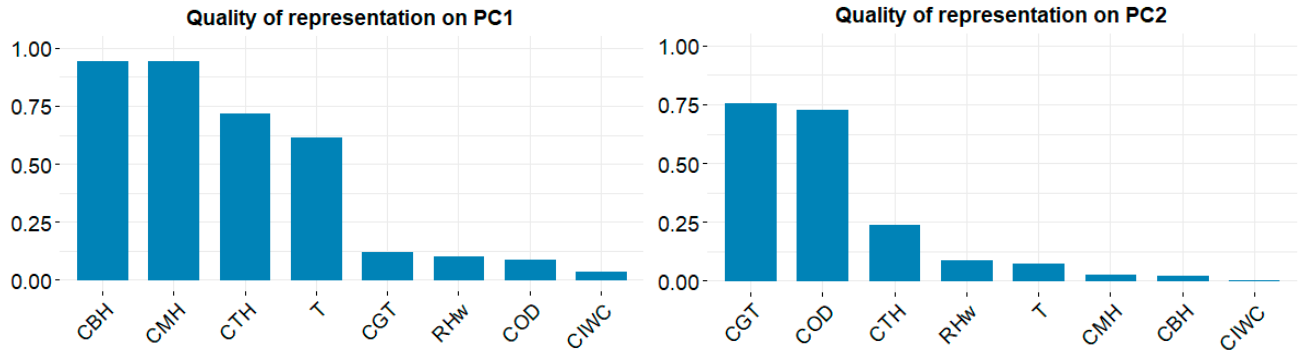

Figure 4. Quality of the representation of all cirrus parameters (CBH, CMH, CTH, CGH, COD, RH_w, T, and CIWC) on the two principal components (PC1 and PC2). The Cos2 function gives the length of the projection of the cirrus parameters on PCs, and so the quality of representation.

The biplot of Figure 5a represents a scatterplot of the PC scores of the individuals. Meanwhile, the variable loadings of the PCA are plotted as arrows in Figure 5b. Parameters that are grouped are positively correlated with each other and vice versa. On the other hand, the greater the vector is, the better that parameter is represented.

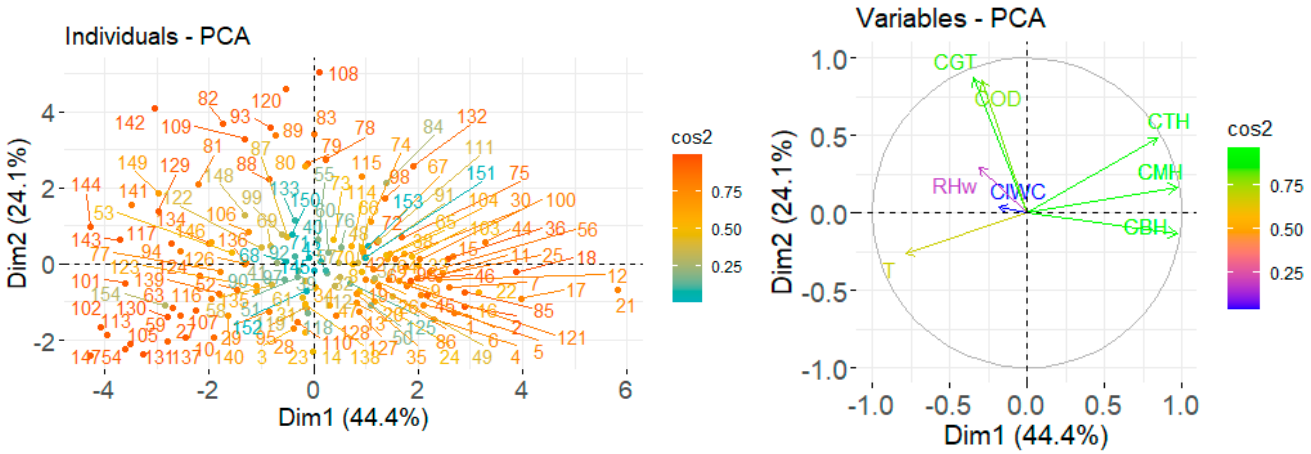

(**a**) (**b**)

Figure 5. Biplots of (**a**) individuals and (**b**) variables. Projection of each of the cloud parameters onto a scatterplot that uses the first two PCs as the axes. Individuals or variables with a similar profile are grouped. The colors indicate their degree of contribution.

Correlation coefficients calculated by using the original variables and also between PCs according to the list of 154 cirrus cases are also shown by the correlation matrix, Figure 6.

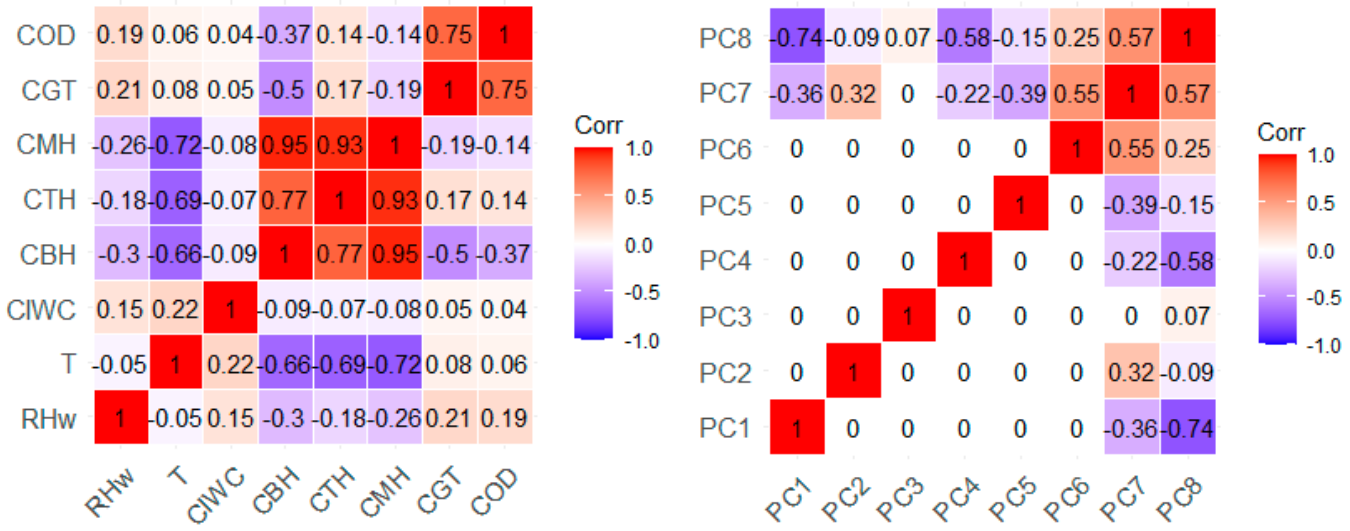

(**a**) (**b**)

Figure 6. (**a**) Pearson correlation matrix among all the variables: temperature, cloud base, mean, and top heights, geometrical and optical depths, temperature, and relative humidity related to water. (**b**) Pearson correlation matrix among the values of the eight principal components.

By comparing the magnitude of the biplot vectors (Figure 5) and the Pearson correlation coefficients (Figure 6), cloud altitude CBH, CMH, and CTH results positively correlated with each other (0.77 ÷ 0.95) and negatively with mid-cloud temperature (−0.66 ÷ 0.72). Furthermore, CGT and COD results positively correlated with each other (0.75). Cloud ice water content in cirrus results slightly correlated with the relative humidity, as higher RH facilitates the growth of ice crystals, leading to higher CIWC. An interesting but weak correlation was identified between CBH and COD and CGT, (−0.37 ÷ −0.50). These values indicate that cirrus with elevated base heights tend to be thinner compared to those with low base heights. The other correlation results are insignificant, except PC7 and PC8, which are of much lesser importance.

3.4. Clustering on PCs—Cirrus Classes

Cluster analysis on the principal components was applied to investigate further cirrus cloud properties and the meteorological parameters. This technique allowed us to reduce the amount of excessive data, by using only the less correlated variables (PCs) and projecting data onto a lower-dimensional space [87]. Here, the number of variables is reduced from 8 down to 2 (considering only PC1 and PC2).

To obtain a more concise determination of the optimal number of clusters, a certain method must be used after applying PCA. Gap statistics is the best choice in the case of correlated data, which is the case with the cirrus properties. It provides a statistically robust comparison to random data, which is important for ensuring that the clusters in the reduced-dimension dataset are meaningful. This method suggests four principal clusters, reaching the maximal gap of 0.42 (Figure 7). The four clusters were provided by the application of two methods: k-means and PAM (Figure 8).

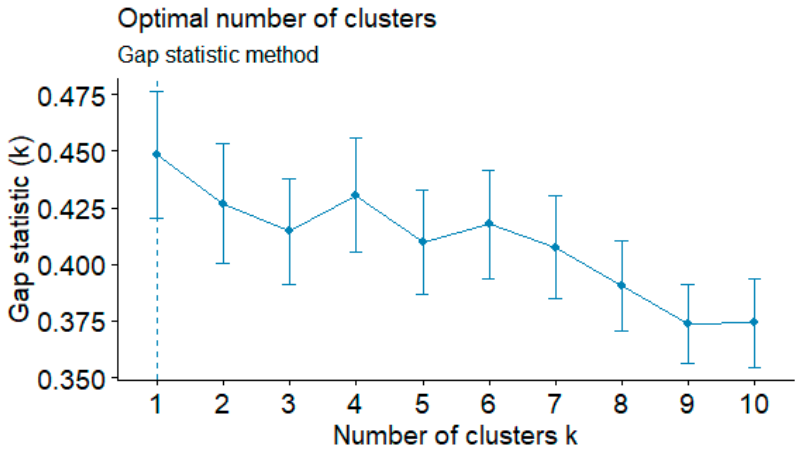

Figure 7. Determination of the optimal number of clusters, based on the gap statistic method. This method suggests 4 principal clusters.

Figure 8. Clustering on PCA results. (**a**) The k-means method and (**b**) PAM method were used to discriminate the cirrus data and to group them into four principal clusters (classes).

Table 6 summarizes the values of the cirrus properties for each class.

Table 6. The properties of the cirrus clouds and their respective occurrences are classified into four classes. The classification was derived from the clustering of PCA results.

Class	CBH (km)	CMH (km)	CTH (km)	CGT (km)	COD	T (°C)	Type	Position	Occur. (%)
K-means clustering (on original data)									
1	11.7	12.2	12.7	1.06	0.20	−61.3	Thin	Tropopause	31.8
2	9.0	10.7	12.5	3.49	1.39	−55.7	Thick	Upper troposphere	11.7
3	10.0	10.6	11.4	1.43	0.24	−54.7	Moderate	Upper troposphere	37.0
4	8.1	8.8	9.6	1.57	0.40	−44.2	Moderate	Mid-troposphere	19.5
PAM clustering (on original data)									
1	11.52	12.04	12.55	1.03	0.19	−60.9	Thin	Tropopause	37.0
2	9.11	10.84	12.58	3.47	1.41	−56.9	Thick	Upper troposphere	11.7
3	9.75	10.53	11.31	1.56	0.27	−53.4	Moderate	Upper troposphere	33.8
4	8.0	8.7	9.5	1.52	0.39	−43.7	Moderate	Mid-troposphere	17.5

Tropopause cirrus (class 1) are situated at an altitude of 12.1 km. This class is the thinnest class in terms of CMH (1.0 km) and COD (0.20). This class is found to be very frequent, about 34%. Upper tropospheric cirrus (class 2) have by far the highest geometrical

and optical depths, a CGT of 3.5 km and a COD of 1.4. However, they are the least common (11.7%). This class is situated in the upper troposphere, CMH 10.7 km, the same as class 3. Nevertheless, class 3 is characterized by a moderate geometrical depth of 1.5 km, a low optical depth of 0.25, and a high occurrence of 35%. The mid-tropospheric layers (class 4) are situated at the lowest altitudes; the CMH is 8.8 km. This class has moderate geometrical depth (1.5 km) and relatively high optical depth (0.40).

Both clustering methods give approximately similar results in the case of the clustering on PCA results, which was not the case for the original data, where these methods differ too much, especially for the COD values. This fact evidences another advantage of the method and strongly recommends the use of the PCA results instead of the original data. PCA simplifies data by reducing their dimensionality, removing noise and less important features, and leaving the most significant components. This makes clustering algorithms more consistent across methods, especially when the original data have correlations or noise.

A schematic visualization of the distribution of the four cirrus classes, derived by k-means and PAM methods and using original data and PCA products, is shown in Figure 9. The classes are better separated in the PCA results compared to the original data, which indicates another advantage of the PCA.

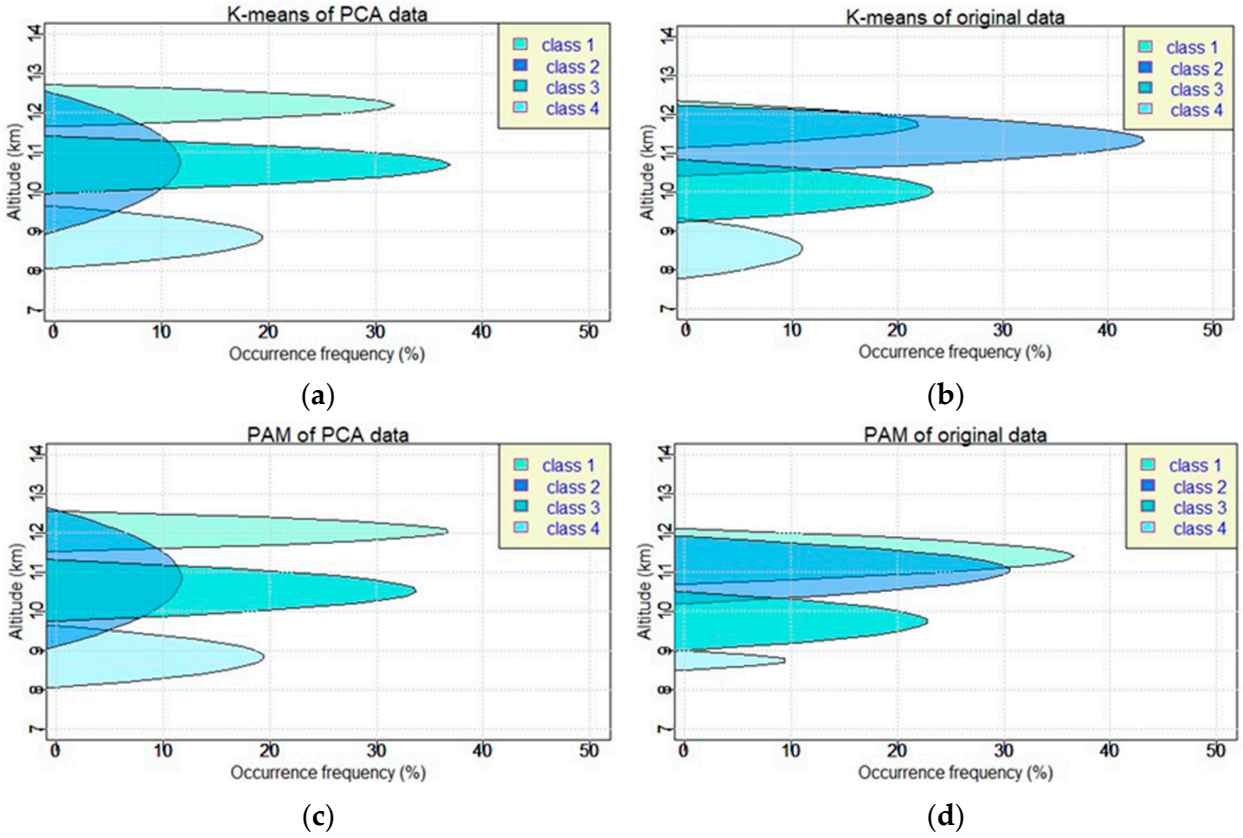

Figure 9. Two clustering approaches, PAM and k-means, offer patterns of the cirrus classes in terms of occurrence frequency and intensity. Visualization based on original data (**b**,**d**) and PCA results (**a**,**c**), using a 2nd degree function as an approximation. The function constants have been determined based on the mean values of CMH, CGT, and frequency of occurrences of cirrus.

The result that stands out the most using the PCA results is the presence of two overlapping cirrus classes (classes 2 and 3). Nevertheless, even though these classes have approximately similar cloud mean heights, their geometrical/optical depths, and also the occurrences, differ too much. Compared to the three-classes scenario, the use of the four-classes scenario gives additional insights into cirrus layer characteristics at these altitudes, making it advantageous [32]. The four-classes information was obtained due to the splitting

of the middle class in the previous three-classes scenario [41,43]. A generalized comparison of the cirrus properties, derived from several studies, is presented in Table 7.

Table 7. Comparison of cirrus characteristics with previous studies. Here, occurrence, mid-cloud height, geometrical and optical depth, and mid-cloud temperature have been compared.

Characteristic	Ref.	Thin MT	Thick UT	Thin UT	Thin TP
Occurrence (%)	This study	19.5	11.7	31.8	37.0
	[32]	17	21	30	30
	[41]	28	30	42	–
	[43]	36	27	35	–
CMH (km)	This study	8.8 ± 0.9	10.7 ± 0.9	12.2 ± 0.7	10.7 ± 0.6
	[32]	7.8 ± 0.9	8.8 ± 0.9	11.2 ± 0.7	10.2 ± 0.9
	[41]	8.1 ± 1.0	10.4 ± 1.0	11.2 ± 1.1	–
	[43]	8.6 ± 0.9	9.8 ± 0.7	11.5 ± 0.9	–
CGT (km)	This study	1.6 ± 0.7	3.5 ± 0.8	1.1 ± 0.5	1.4 ± 0.5
	[32]	1.2 ± 0.7	4.3 ± 0.8	1.3 ± 0.5	2.8 ± 0.6
	[41]	1.3 ± 0.8	2.9 ± 1	1.0 ± 0.4	–
	[43]	0.9 ± 0.8	3.2 ± 0.9	0.9 ± 0.6	–
COD	This study	0.2 ± 0.8	1.0 ± 0.8	0.1 ± 0.2	0.2 ± 1.0
	[32]	0.04 ± 0.06	0.47 ± 0.36	0.09 ± 0.09	0.16 ± 0.20
	[41]	0.1 ± 0.2	0.5 ± 0.4	0.07 ± 0.06	–
	[43]	0.2 ± 0.2	0.8 ± 0.4	0.1 ± 0.1	–
T (°C)	This study	-44.2 ± 4.0	-55.7 ± 5.1	-61.3 ± 4.2	-54.7 ± 5.0
	[32]	-36 ± 7	-42 ± 7	-58 ± 4	-53 ± 4
	[41]	-38 ± 9	-52 ± 6	-56 ± 7	–
	[43]	-41 ± 6	-50 ± 6	-58 ± 6	–

The statistical interpretation of each of the cirrus microphysical properties is given by the analysis of the boxplots of the relative humidity and the cloud ice water content (Figure 10).

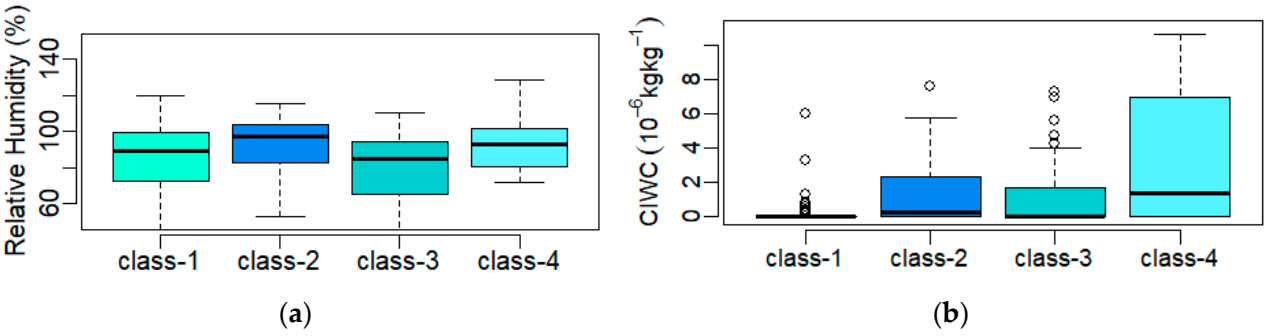

Figure 10. Boxplots of the distribution of (**a**) relative humidity and (**b**) cloud ice water content, for each of the four cirrus classes. Different colors are used to identify each of the classes.

A strong correlation (0.93) was revealed between the class variations in the RH and CIWC values. However, both these microphysical parameters show nonuniform variations among the cirrus classes, with mid-tropospheric cirrus characterized by the highest values.

3.5. Optical Properties—Cirrus Groups

Another point of view is the categorization of the cirrus clouds according to their optical properties. In terms of cloud optical depth, three cirrus groups were identified: subvisible, thin, and opaque. We observed only 5.2% subvisible cirrus (COD < 0.03), 57.1% thin cirrus (0.03 < COD < 0.3), and 37.7% thick cirrus (0.3 < COD). Table 8 shows the comparative results with other studies.

Table 8. Comparison of the percentages of cirrus optical groups from various studies.

SVC	Thin	Thick	Visible	Opaque	Reference
Comparable results					
5	57	38	95	38	This study
3	57	40	97	40	[31]
10	49	41	90	41	[32]
10	65	25	90	25	[88]
14	48	38	86	38	[36]
32	51	17	82	17	[33]
Less similar results					
42	38	20	77	20	[48]
43	46	11	68	11	[33]
35	52	13	62	13	[33]
–	–	–	67	–	[51]
–	–	–	50	–	[13]

The majority of subvisible cirrus are situated at high altitudes. So, 62.5% of them are situated in the tropopause (class 1) and 37.5% in the upper troposphere (class 3). Cirrus clouds found at elevated altitudes originate from air masses possessing limited water vapor content, resulting in low geometric and optical depths. Thin clouds are found in 37.5% of the cases in the tropopause and 42.0% in the upper troposphere. Meanwhile, opaque cirrus are found mostly in the upper and mid-troposphere.

Class 1 consists mostly of thin cirrus (67.3%) and less of opaque cirrus (22.4%). Class 2 consists almost completely of opaque cirrus (94.4%). Meanwhile, both thin and opaque cirrus contributes to classes 3 and 4, by 64.9% and 29.8%, and 53.3% and 46.7%, respectively.

SVC cirrus are found at the highest altitudes, whilst the opaque are the lowest. Regarding cloud depths, CGT and COD display a gradual increase from SVC to opaque cirrus. SVC resulted in much lower CIWC compared to visible cirrus.

The compact information in Table 9 shows the parameters of the groups. Tropospheric cirrus come out geometrically and optically thicker and have a higher temperature, relative humidity, and cloud ice water content than those situated in the tropopause. Especially, upper tropospheric opaque cirrus have the lowest height and the highest geometrical and optical depths, temperature, and relative humidity. Meanwhile, tropopause CVC clouds, being generally the coldest and thinnest, exhibit the lowest values of COD and have the lowest RH and CIWC.

Table 9. Mean cloud heights, geometrical and optical depths, cloud ice water content, vertical velocity (ω), mid-cloud temperature, and relative humidity (RH) among cirrus optical groups.

	CBH	CMH	CTH	CGT	COD	CIWC	ω	T	RH
SVC	11.4	11.7	11.9	0.5	0.02	7.4×10^{-7}	0.024	−58.8	68.6
Thin	10.3	11.0	11.6	1.2	0.15	2.8×10^{-6}	0.015	−54.9	78.3
Opaque	9.3	10.5	11.6	2.3	0.81	2.7×10^{-6}	0.004	−54.3	90.3

Even though the correlation coefficients of the COD and other properties are statistically low, a significant correlation between COD and CIWC of 0.58 was found for the subvisible cirrus group, which explains the impact of the ice content within the thinnest cirrus on their optical depth. Both cirrus groups have very low vertical velocities ($4 - 24 \times 10^{-3}$ Pa·s^{-1}), which suggests a mixing state between ascending and descending motions. Based on the mean vertical velocity, which explains the large-scale dynamics of the atmosphere, opaque cirrus clouds tend to be characterized by more stable synoptic conditions compared to the thinnest ones. Ascending motion will lower the cirrus base height and raise the cloud top, which lifts particles to higher altitudes, deepens the supersaturation layer via adiabatic cooling, and maintains the growth of ice crystal particles to

larger sizes through the water vapor deposition and aggregation processes until they fall out the supersaturated layer [88,89].

3.6. Seasonal Variations of the Cirrus Classes and Groups

Because both clustering methods provided very close results applying to PCA outputs, for simplicity only the k-means will be taken into account in this section. The seasonal occurrences of the cirrus cloud have been analyzed to have a clear picture of their annual variation (Figure 11).

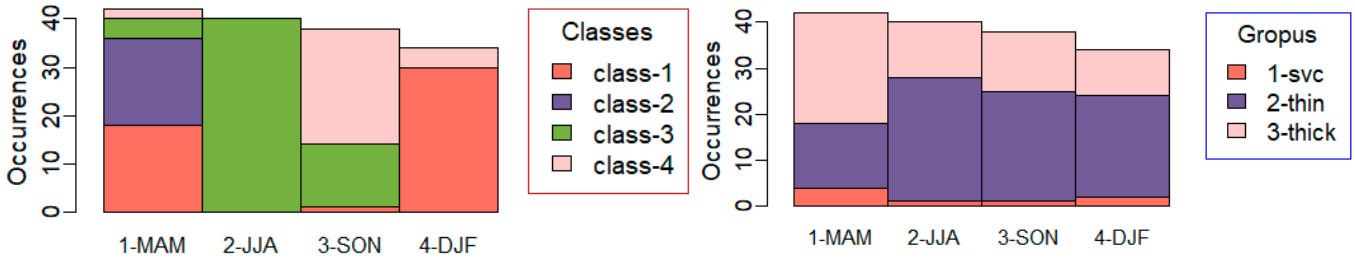

(**a**) (**b**)

Figure 11. Seasonal variation in the cirrus cloud events over the OHP site. Occurrences of all cirrus cases grouped according to (**a**) cirrus classes and (**b**) cirrus groups are presented.

The tropopause cirrus clouds are more evident during winter and spring, possibly due to the colder temperatures and increased atmospheric instability during these seasons; the upper tropospheric cirrus appear more in summer and less in autumn, related to the warm, moist air that rises during summer, leading to more cloud formation. Meanwhile, mid-tropospheric cirrus dominate the autumn season.

Regarding the seasonal variation in the occurrences of cirrus groups, SVC occurrence remains very low, peaking in spring, similar to the opaque group. Thin cirrus clouds are more frequent during the summer season, due to the abundance of moisture and warm air, which favors the formation of thin, wispy clouds. Comparable results were also obtained from [36,37,41].

In terms of the monthly occurrences of all the cirrus classes/groups taken together, two distinct maximums have been observed: in May and during September–October. These two periods correspond to the maximums in the spring and autumn seasons, in agreement with satellite climatologies, and as suggested by other studies [33,36,41,51]. During winter, low-level clouds often block the laser from reaching potential cirrus clouds, resulting in a lower frequency of lidar measurements [31]. Monthly and seasonal variations in the cirrus occurrences reveal that the thin tropopause cirrus are strongly affected by the presence of the upper tropospheric cirrus, by reducing deep convection and the lidar detection efficiency of high-level clouds [40].

The variations in cloud heights, depths, and occurrence frequencies according to the four classes and three cirrus groups have also been investigated to obtain conclusive evidence on the seasonal variation in the cirrus properties (Table 10).

Cirrus heights reach their maximum during the winter–spring seasons, associated with a CMH of 11.3 km during MAM and 11.8 km in DJF. Higher cirrus heights during these seasons could reflect a stronger influence of cold dry air aloft and the presence of more robust atmospheric lifting mechanisms, indicating the impact of the lower temperatures and increased atmospheric instability. The lowest cirrus heights were obtained during autumn (a CMH of 9.5 km), indicating a more stable atmosphere or changes in temperature profiles that do not favor the development of high-altitude clouds during this transition period. Meanwhile, during the summer season, intermediate cloud heights are more evident.

Table 10. Seasonal variations in CBH, CMH, CTH, CGT, COD, and T. Also, the seasonal percentage occurrences of each cirrus class and group are presented.

Season	CBH (km)	CMH (km)	CTH (km)	CGT (km)	COD	T (°C)	Frequency (%)
MAM	10.2	11.3	12.3	2.06	0.70	−57.8	27.9
JJA	9.9	10.7	11.4	1.50	0.25	−54.5	26.0
SON	8.8	9.5	10.3	1.50	0.34	−47.3	24.7
DJF	11.2	11.8	12.4	1.15	0.23	−60.3	21.4
	Class 1	**Class 2**	**Class 3**	**Class 4**	**SVC**	**Thin**	**Opaque**
MAM	12.3	11.7	2.6	1.3	2.6	9.7	15.6
JJA	–	–	26.0	–	0.6	17.5	7.8
SON	–	–	8.4	16.2	0.6	14.9	9.1
DJF	19.5	–	–	1.9	1.3	14.3	5.8

Regarding the cloud depth, the spring season produces heavily thick cirrus, associated with much higher CGT (2.1 km) and COD (0.70) compared to the other seasons, which in turn have approximate cirrus mean seasonal depths. SVC and opaque, but not thin, cirrus occur mostly in spring.

In the northern mid-latitudes, the rapid upward movement of warm air masses, forming thick cirrus clouds, is most frequent in spring. Increased solar heating during this season heightens atmospheric instability, making such phenomena more likely. During spring, stark differences between cold and warm air masses create robust frontal systems and the substantial upward movement of warm air. Synoptic-scale weather phenomena, in particular jet streams, frontal systems, and upper-level troughs, remain key drivers of cirrus cloud formation throughout the year. However, summer relies more on convective processes and high-altitude outflows (anvil cirrus), while winter and autumn are dominated by large-scale lifting mechanisms, like cyclones, strong jet streams, and frontal systems [33].

Summing up, the occurrence of cirrus clouds varies seasonally due to the complex interplay of temperature, humidity, atmospheric circulation, solar radiation, weather patterns, and geographical location [90]. Thus, seasonal variations in temperature, solar radiation, humidity levels, atmospheric general circulation, large-scale weather systems, etc., affect differently the formation of each of the cirrus classes and groups [91].

3.7. Categorization Based on the Cirrus Mechanism of Formation

Atmospheric processes affect the characteristics of cirrus that form. Consequently, cooling at the tropopause height causes subvisible cirrus clouds to form, whereas thick cirrus clouds are often created at lower heights by deep convective outflow, except deep overshooting convections [92]. The so-called lenticularis cirrus, which are thicker than large-scale cirrus clouds but thinner than the cirrus created as an outflow of anvils or in warm conveyor belts, are often the result of the orography-driven lifting of air masses.

Other recent studies have included the mechanism of cirrus formation as a useful tool for their classification. Two main categories have been determined: in situ and liquid-origin cirrus [16,19]. Thus, in situ origin cirrus have been categorized as thin and high cirrus of COD < 1 and CIWC < 10^{-6} kg·m^{-3}, meanwhile, those of liquid origin are thicker and of lower altitude, COD > 1 and CIWC > 10^{-6} kg·m^{-3}. In situ cirrus can be split further into two distinct categories: slow in situ and fast in situ [11,16]. Slow in situ cirrus clouds form gradually under slow vertical motions (updraft 10 cm·s^{-1}), typically associated with large-scale processes like synoptic-scale lifting, while fast in situ cirrus clouds form rapidly (updraft 10 cm·s^{-1}), often due to rapid vertical motions such as those found near convective outflows or in jet streams. Slow in situ have smaller optical depth (COD 0.001–0.05) compared to the fast in situ cirrus (COD 0.05–1.0). According to [19], cirrus clouds formed in situ are more prevalent at temperatures below −55 °C, whereas liquid-origin cirrus are more common at higher temperatures.

In addition, the density distribution of the CIWC shows a maximal peak at 9.3×10^{-8} kg·kg^{-1}, which belongs mainly to the in situ cirrus, followed by multiple lower peaks at higher CIWC also pertaining to the liquid-origin cirrus category. The mean values of the cirrus properties classified by their mechanism of formation are given in Table 11.

Table 11. Mean parameters of the cirrus categories in situ (slow and fast) and liquid–origin cirrus.

	CIWC	CBH	CMH	CTH	CGT	COD	RH	T	Occurr.
Slow in situ	6.5×10^{-7}	11.1	11.4	11.8	0.70	0.05	−57.9	79.4	9.1
Fast in situ	3.4×10^{-7}	10.2	11.0	11.8	1.62	0.42	−56.5	80.5	72.1
In situ both	3.8×10^{-7}	10.3	11.0	11.8	1.52	0.36	−56.7	80.3	81.2
Liquid origin	8.4×10^{-6}	7.8	9.2	10.6	2.78	1.14	−44.3	108.9	5.2
Other cases	1.4×10^{-5}	9.5	10.2	10.9	1.48	0.22	−48.4	84.8	13.6

The majority of cirrus clouds, about 72.1% of them, result from fast in situ origin, 9.1% from slow in situ, and only 5.2% from liquid origin. Meanwhile, the remaining 13.6% of the cases cannot be classified applying only these conditions, named undefined. Table 11's mean data indicate that, in comparison to in situ cirrus, liquid-origin cirrus have higher CIWC and COD and are located at lower altitudes, higher temperatures, and higher relative humidity conditions.

The liquid-origin cirrus category is composed of only thick cirrus, while in situ cirrus occurs in all cirrus groups. Even though the slow in situ category does not contain opaque cirrus (57% CVC and 43% thin), the fast in situ cirrus are also composed by thicker cirrus (57.7% thin and 42.3% opaque).

Both the CIWC and COD criteria were taken into account when evaluating this undefinable category. Mean CIWC ($1.4 \times 10^{-5} < 1.0 \times 10^{-6}$) is extremely large, which is a feature of the liquid–origin cirrus. However, the low mean COD (0.22 < 1.0) suggests the in situ origin. The mean altitude (10.2 km) of this category is an intermediate value of the liquid-origin (9.2 km) and in situ cirrus (11.0 km), which does not allow us to have a clear idea of what origin it belongs to. The mean temperature (−48.4 °C) is lower than the limit of −55 °C, which suggests again that the majority of this category belongs to the liquid-origin cirrus [19]. To better categorize this undefined category, a trajectory-based approach is advisable, even though it was not conducted in this study [93].

The frequency distribution of the cirrus cases by their temperature demonstrates disparities between that of the in situ cirrus and other cases taken together (Figure 12). In situ cirrus, both slow and fast, as is expected, show a distribution peaking at temperatures lower than 50 °C. Meanwhile, the mode of the frequency distribution of other cases (liquid + undetermined) is shifted toward higher temperatures than 50 °C, suggesting the predominance of the liquid-origin cirrus. A similar bimodal distribution of temperatures was obtained previously over the OHP, situated, respectively, at −45 °C and −60 °C [43].

At this point, cirrus have been classified threefold concerning their properties and history. The overall picture of the cirrus triple classification is demonstrated in Table 12.

The final results regarding the main characteristics of the four cirrus classes found beforehand can be summarized as follows. The mid-tropospheric layer is composed of almost visible cirrus, but of undetermined origin. The thinner upper tropospheric layer contains mostly thin cirrus (65%) of in situ origin (57%). The thicker upper tropospheric layer consists of nearly exclusively opaque cirrus (91%), which has equal levels of liquid- and in situ origin. In the thin upper tropospheric layer, the tropopause cirrus are composed mainly of thin cirrus (62%) of in situ origin (74%).

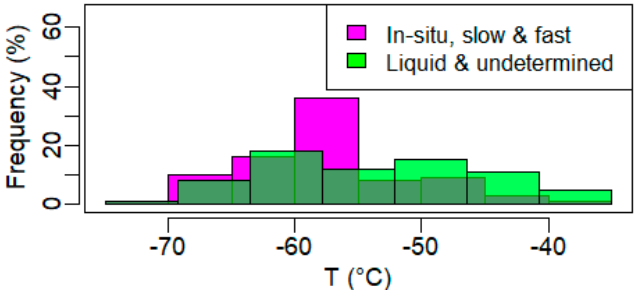

Figure 12. Frequencies of the occurrence of the in situ origin cirrus (comprising the slow and fast uplifting categories) and the liquid-origin cirrus (including the remaining undefined cases).

Table 12. General classification scheme of the cirrus clouds based on the three perspective: cirrus geometrical morphology, optical depth, and formation history.

Morphology (4 Classes)	Optical Properties (3 Groups)	Formation Mechanisms (3 Categories)
Mid-tropospheric	Subvisible	Slow in situ
Thick upper-tropospheric	Thin	Fast in situ
Thin upper-tropospheric	Opaque	Liquid
Tropopause cirrus		

To have a better visualization of the co-occurrences of the different cirrus categories, a Chord diagram and an Alluvial diagram are created in Figure 13.

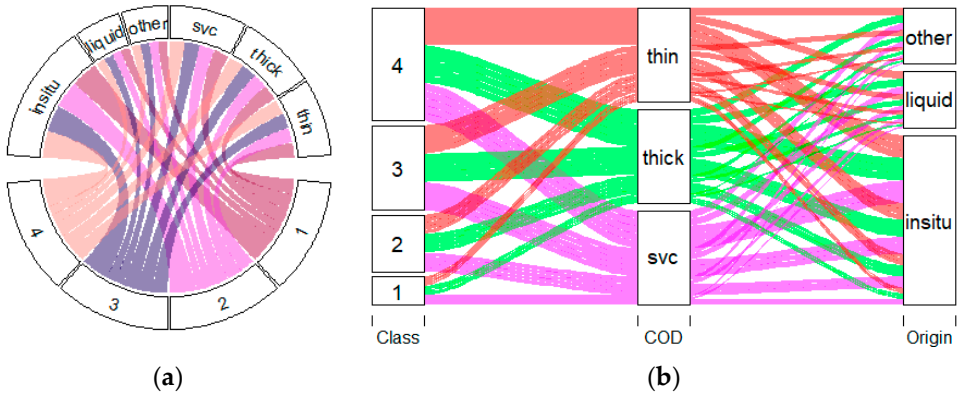

(**a**) (**b**)

Figure 13. Interconnections among different cirrus categorizations. (**a**) Chord diagram indicating the strength of the relationship between three cirrus classifications. (**b**) Alluvial diagram connecting all cirrus categories. each of the diagram colors represent a linkage between different cirrus categorizations.

The thicker chords of the Chord diagram (Figure 13a) represent stronger connections between categories. The strongest relationships are those connecting upper tropospheric with in situ origin cirrus clouds. After that, a very strong correlation is demonstrated between upper tropospheric cirrus with thin clouds and tropopause cirrus with in situ origin clouds. On the other hand, the Alluvial diagram in Figure 13b suggests that thin cirrus of the fast in situ origin located in the upper tropospheric and tropopause regions have a major connection. At European mid-latitudes, the most common cirrus clouds are associated with slow updrafts in frontal systems and include both liquid-origin and in situ origin cirrus [11,16]. However, in this study, fast updrafts in frontal systems were revealed to be the most predominant cirrus formation mechanism over the OHP.

Because we are focusing on the characteristics of cirrus clouds (such as the occurrence, optical depth, altitude, etc.) and observing their seasonal variations, this period could be sufficient, especially if the data are high-resolution, which it is in our case with 160 s

temporal resolution. However, a longer period should be taken into consideration for a robust climatology of long-term cirrus patterns.

4. Conclusions

About three years of ground-based lidar observations at the Observatory of Haute-Provence, France, were used in this study to perform a cross-classification based on geometrical, microphysical, and optical features of the cirrus cloud. A multivariate analysis was carried out, combining the cluster analysis with principal component analysis of the cirrus properties. Cloud geometrical and optical depths, as well as cloud base, mid, and top heights, were considered. Additional parameters, such as temperature, relative humidity and cloud ice water content, vertical velocity, etc., have been provided by ERA5 reanalysis.

The overall results are comparable with the previous studies in the mid-latitude regions, even though new findings have been obtained. One important finding is that clustering on the principal components instead of on the original parameters gives more accurate and robust results on the classification of the cirrus properties, and makes the selection of different clustering methods less difficult to determine. Cirrus clouds were identified in about 37% of the total observation time. Only 33.3% of these cirrus cases had a multi-layer structure, whereas the majority (66.7%) had a single-layer structure. The mean cloud optical depth found in this study was 0.39. Mean values of the base-, mid- and top-cloud height were 10.0, 10.8, and 11.6 km, respectively. The mid-cloud temperature was -54.9 °C. The mean cloud geometrical depth was 1.6 km. High correlations have been estimated between cirrus cloud base, mid, and top height, 0.77 ± 0.95, as well as an inverse correlation of mid-cloud temperature with all the cloud heights (-0.66 to 0.72). Furthermore, a high correlation of 0.75 between geometrical and optical depths was identified as well.

Based on their morphology, cirrus clouds have been classified into four main classes: one mid-tropospheric, two upper-tropospheric, and another tropopause cirrus class. In addition, based on their optical properties, cirrus have been classified into three main groups: subvisible, thin and opaque. The amounts of these cirrus groups are less subvisible cirrus with 5.2%, more thin cirrus with 57.1%, and 37.7% of thick cirrus. Visible cirrus clouds are predominant compared to the subvisible cirrus, which are generally situated at higher altitudes.

The tropospheric cirrus clouds exhibit greater geometric and optical depth, along with higher temperatures, relative humidity, and ice water content compared to those found in the tropopause. Because of the more favorable synoptic conditions, opaque cirrus results are more stable compared to thinner cirrus. Seasonal variations in cirrus occurrences reach a maximum during spring. Significant correlations between cirrus class occurrences reveal that cirrus layers influence each other in multi-layered structures.

The final step also included categorizing cirrus clouds according to the mechanism of their formation. The upper tropospheric and tropopause thin cirrus belong to the in situ origin, while the opaque upper tropospheric layer is mainly of uplifted liquid-origin, generally related to the frontal systems. The lowest mid-tropospheric cirrus were mainly visible but of an uncertain mechanism of formation. The most frequently occurring scenario is that of the upper tropospheric thin cirrus clouds formed in situ.

In summary, cirrus clouds have been classified in multiple ways, with the main categories determined by their geometric, optical, and formation history features. The climatology of the cirrus types and appropriate comparative analysis with previous studies were performed. Our results highlight the complex interplay between atmospheric conditions and cloud formation.

Author Contributions: Conceptualization, P.K.; methodology, F.M., D.A. and A.S.; software, S.K.; validation, P.K and F.M.; formal analysis, F.M.; investigation, F.M, S.K and A.S.; resources, P.K.; data curation, F.M. and S.K.; writing—original draft preparation, F.M.; writing—review and editing, D.A., S.K and A.S.; visualization, F.M.; supervision, P.K.; project administration, P.K.; funding acquisition, P.K. All authors have read and agreed to the published version of the manuscript.

Funding: This project has received funding from the French government (BPI) in the frame of France 2030 under Grant DOS0182433/00 for the CONTRAILS project and from the Horizon Europe Research and Innovation Actions program under Grant Agreement N°101056885 through the BeCoM (Better Contrail Mitigation) project.

Institutional Review Board Statement: Not applicable.

Informed Consent Statement: Not applicable.

Data Availability Statement: Publicly available datasets were analyzed in this study.

Conflicts of Interest: The authors declare no conflict of interest.

References

1. Sassen, K.; Wang, Z.; Liu, D. Global distribution of cirrus clouds from CloudSat/cloud-aerosol lidar and infrared pathfinder satellite observations (CALIPSO) measurements. *J. Geophys. Res.-Atmos.* **2008**, *113*, D00A12. [CrossRef]
2. Li, Q.; Jiang, J.H.; Wu, D.L.; Read, W.G.; Livesey, N.J.; Waters, J.W.; Zhang, Y.; Wang, B.; Filipiak, M.J.; Davis, C.P. Convective outflow of South Asian pollution: A global CTM simulation compared with EOS MLS observations. *Geophys. Res. Lett.* **2005**, *32*, L14826. [CrossRef]
3. Fu, R.; Hu, Y.; Wright, J.S.; Jiang, J.H.; Dickinson, R.E.; Chen, M.; Filipiak, M.; Read, W.G.; Waters, J.W.; Wu, D.L. Short circuit of water vapor and polluted air to the global stratosphere by convective transport over the Tibetan Plateau. *Proc. Natl. Acad. Sci. USA* **2006**, *103*, 5664–5669. [CrossRef]
4. Jin, M.L. MODIS observed seasonal and interannual variations of atmospheric conditions associated with hydrological cycle over Tibetan Plateau. *Geophys. Res. Lett.* **2006**, *33*, L19707. [CrossRef]
5. Chen, B.; Liu, X. Seasonal migration of cirrus clouds over the Asian Monsoon regions and the Tibetan Plateau measured from MODIS/Terra. *Geophys. Res. Lett.* **2005**, *32*, L01804. [CrossRef]
6. Spichtinger, P.; Gierens, K.; Leiterer, U.; Dier, H. Ice supersaturation in the tropopause region over Lindenberg, Germany. *Meteorol. Z.* **2003**, *12*, 143–156. [CrossRef]
7. Berry, E.; Mace, G.G. Cirrus Cloud Properties and the Large-Scale Meteorological Environment: Relationships Derived from A-Train and NCEP–NCAR Reanalysis Data. *J. Appl. Meteorol. Climatol.* **2013**, *52*, 5. [CrossRef]
8. Muhlbauer, A.; Ackerman, T.P.; Comstock, J.M.; Diskin, G.S.; Evans, S.M.; Lawson, R.P.; Marchand, R.T. Impact of large-scaledynamics on the microphysical properties of midlatitude cirrus. *J. Geophys. Res. Atmos.* **2014**, *119*, 3976–3996. [CrossRef]
9. Wolf, K.; Bellouin, N.; Boucher, O. Long-term upper-troposphere climatology of potential contrail occurrence over the Paris area derived from radiosonde observations. *Atmos. Chem. Phys.* **2023**, *23*, 287–309. [CrossRef]
10. Voigt, C.; Schumann, U.; Minikin, A.; Abdelmonem, A.; Afchine, A.; Borrmann, S.; Boettcher, M.; Buchholz, B.; Bugliaro, L.; Costa, A.; et al. ML-CIRRUS: The airborne experiment on natural cirrus and contrail cirrus with the high-altitude long-range research aircraft HALO. *Bull. Am. Meteorol. Soc.* **2017**, *98*, 271–288. [CrossRef]
11. Krämer, M.; Rolf, C.; Spelten, N.; Afchine, A.; Fahey, D.; Jensen, E.; Khaykin, S.; Kuhn, T.; Lawson, P.; Lykov, A.; et al. A microphysics guide to cirrus—Part 2: Climatologies of clouds and humidity from observations. *Atmos. Chem. Phys.* **2020**, *20*, 12569–12608. [CrossRef]
12. Kim, Y.; Kim, S.W.; Kim, M.H.; Yoon, S.C. Geometric and optical properties of cirrus clouds inferred from three-year ground-based lidar and CALIOP measurements over Seoul, Korea. *Atmos. Res.* **2014**, *139*, 27–35. [CrossRef]
13. Sassen, K.; Campbell, J.R. A midlatitude cirrus cloud climatology from the facility for atmospheric remote sensing. Part I: Macrophysical and synoptic properties. *J. Atmos. Sci.* **2001**, *58*, 481–496. [CrossRef]
14. Sassen, K.; Comstock, J.M. A midlatitude cirrus cloud climatology from the facility for atmospheric remote sensing. Part III: Radiative properties. *J. Atmos. Sci.* **2001**, *58*, 2113–2127. [CrossRef]
15. Desbois, M.; Seze, G.; Szejwach, G. Automatic classification of clouds on METEOSAT imagery: Application to high-level clouds. *J. Appl. Meteor.* **1982**, *21*, 401–412. [CrossRef]
16. Krämer, M.; Rolf, C.; Luebke, A.; Afchine, A.; Spelten, N.; Costa, A.; Meyer, J.; Zöger, M.; Smith, J.; Herman, R.L.; et al. A microphysics guide to cirrus clouds—Part 1: Cirrus types. *Atmos. Chem. Phys.* **2016**, *16*, 3463–3483. [CrossRef]
17. Luebke, A.E.; Afchine, A.; Costa, A.; Grooß, J.-U.; Meyer, J.; Rolf, C.; Spelten, N.; Avallone, L.M.; Baumgardner, D.; Krämer, M. The origin of midlatitude ice clouds and the resulting influence on their microphysical properties. *Atmos. Chem. Phys.* **2016**, *16*, 5793–5809. [CrossRef]
18. Wernli, H.; Boettcher, M.; Joos, H.; Miltenberger, A.K.; Spichtinger, P. A trajectory-based classification of ERA-Interim ice clouds in the region of the North Atlantic storm track. *Geophys. Res. Lett.* **2016**, *43*, 6657–6664. [CrossRef]
19. Gasparini, B.; Meyer, A.; Neubauer, D.; Münch, S.; Lohmann, U. Cirrus Cloud Properties as Seen by the CALIPSO Satellite and ECHAM-HAM Global Climate Model. *J. Clim.* **2018**, *31*, 1983–2003. [CrossRef]
20. Urbanek, B.; Groß, S.; Schäfler, A.; Wirth, M. Determining stages of cirrus evolution: A cloud classification scheme. *Atmos. Meas. Tech.* **2017**, *10*, 1653–1664. [CrossRef]
21. Klett, J.D. Stable analytical inversion solution for processing lidar returns. *Appl. Opt.* **1981**, *20*, 211–220. [CrossRef] [PubMed]
22. Fernald, F.G. Analysis of atmospheric lidar observations; some comments. *Appl. Opt.* **1984**, *23*, 652–653. [CrossRef] [PubMed]

23. Ansmann, A.; Wandinger, U.; Riebesell, M.; Weitkamp, C.; Michaelis, W. Independent measurement of extinction and backscatter profiles in cirrus clouds by using a combined Raman elastic-backscatter lidar. *App. Opt.* **1992**, *31*, 7113–7131. [CrossRef] [PubMed]
24. Ansmann, A.; Bosenberg, J.; Brogniez, G.; Elouragini, S.; Flamant, P.H.; Klapheck, K.; Linn, H.; Menenger, L.; Michaelis, W.; Riebesell, M.; et al. Lidar network observations of cirrus morphological and scattering properties during the International Cirrus Experiment 1989. *J. App. Meteor.* **1993**, *32*, 1608–1622. [CrossRef]
25. Gobbi, G.P.; Barnaba, F.; Ammannato, L. The vertical distribution of aerosols, Saharan dust and cirrus clouds in Rome (Italy) in the year 2001. *Atmos. Chem. Phys.* **2004**, *4*, 351–359. [CrossRef]
26. Granados-Muñoz, M.J.; Navas-Guzmán, F.; Bravo-Aranda, J.A.; Guerrero-Rascado, J.L.; Lyamani, H.; Valenzuela, A.; Titos, G.; Fernández-Gálvez, J.; Alados-Arboledas, L. Hygroscopic growth of atmospheric aerosol particles based on active remote sensing and radiosounding measurements: Selected cases in southeastern Spain. *Atmos. Meas. Tech.* **2015**, *8*, 705–718. [CrossRef]
27. Comerón, A.; Muñoz-Porcar, C.; Rodríguez-Gómez, A.; Sicard, M.; Dios, F.; Gil-Díaz, C.; dos Santos Oliveira, D.C.F.; Rocadenbosch, F. An explicit formulation for the retrieval of the overlap function in an elastic and Raman aerosol lidar. *Atmos. Meas. Tech.* **2023**, *16*, 3015–3025. [CrossRef]
28. Granados-Muñoz, M.J.; Sicard, M.; Papagiannopoulos, N.; Barragán, R.; Bravo-Aranda, J.A.; Nicolae, D. Two-dimensional mineral dust radiative effect calculations from CALIPSO observations over Europe. *Atmos. Chem. Phys.* **2019**, *19*, 13157–13173. [CrossRef]
29. Mandija, F.; Guerrero-Rascado, J.L.; Lyamani, H.; Granados-Muñoz, M.J.; Alados-Arboledas, L. Synergic estimation of columnar integrated aerosol properties and their vertical resolved profiles in respect to the scenarios of dust intrusions over Granada. *Atmos. Environ.* **2016**, *145*, 439–454. [CrossRef]
30. Mandija, F.; Markowicz, K.; Zawadzka, O. Characterization of aerosol events using synergistically column integrated optical aerosol properties and polarimetric measurements. *J. Atmos. Sol. -Terr. Phys.* **2016**, *150*, 9–20. [CrossRef]
31. Giannakaki, E.; Balis, D.S.; Amiridis, V.; Kazadzis, S. Optical and geometrical characteristics of cirrus clouds over a Southern European lidar station. *Atmos. Chem. Phys.* **2007**, *7*, 5519–5530. [CrossRef]
32. Dionisi, D.; Keckhut, P.; Liberti, G.L.; Cardillo, F.; Congeduti, F. Midlatitude cirrus classification at Rome Tor Vergata through a multichannel Raman-Mie-Rayleigh lidar. *Atmos. Chem. Phys.* **2013**, *13*, 11853–11868. [CrossRef]
33. Kienast-Sjögren, E.; Rolf, C.; Seifert, P.; Krieger, U.K.; Luo, B.P.; Krämer, M.; Peter, T. Climatological and radiative properties of midlatitude cirrus clouds derived by automatic evaluation of lidar measurements. *Atmos. Chem. Phys.* **2016**, *16*, 7605–7621. [CrossRef]
34. Bartolome Garcia, I.; Spang, R.; Ungermann, J.; Griessbach, S.; Krämer, M.; Höpfner, M.; Riese, M. Observation of cirrus clouds with GLORIA during the WISE campaign: Detection methods and cirrus characterization. *Atmos. Meas. Tech.* **2021**, *14*, 3153–3168. [CrossRef]
35. Voigt, C.; Schumann, U.; Jessberger, P.; Jurkat, T.; Petzold, A.; Gayet, J.-F.; Krämer, M.; Thornberry, T.; Fahey, D.W. Extinction and optical depth of contrails. *Geophys. Res. Lett.* **2011**, *38*, L11806. [CrossRef]
36. Gil-Díaz, C.; Sicard, M.; Comerón, A.; dos Santos Oliveira, D.C.F.; Muñoz-Porcar, C.; Rodríguez-Gómez, A.; Lewis, J.R.; Welton, E.J.; Lolli, S. Geometrical and optical properties of cirrus clouds in Barcelona, Spain: Analysis with the two-way transmittance method of 4 years of lidar measurements. *Atmos. Meas. Tech.* **2024**, *17*, 1197–1216. [CrossRef]
37. Goldfarb, L.; Keckhut, P.; Chanin, M.-L.; Hauchecorne, A. Cirrus climatological results from lidar measurements at OHP (44_ N, 6_ E). *Geophys. Res. Lett.* **2001**, *28*, 1687–1690. [CrossRef]
38. Campbell, J.R.; Vaughan, M.A.; Oo, M.; Holz, R.E.; Lewis, J.R.; Welton, E.J. Distinguishing cirrus cloud presence in autonomous lidar measurements. *Atmos. Meas. Tech.* **2015**, *8*, 435–449. [CrossRef]
39. Eguchi, N.; Yokota, T.; Inoue, G. Characteristics of cirrus clouds from ICESat/GLAS observations. *Geophys. Res. Lett.* **2007**, *34*, L09810. [CrossRef]
40. Dupont, J.-C.; Haeffelin, M.; Morille, Y.; Noël, V.; Keckhut, P.; Winker, D.; Comstock, J.; Chervet, P.; Roblin, A. Macrophysical and optical properties of midlatitude cirrus clouds from four ground-based lidars and collocated CALIOP observations. *J. Geophys. Res.* **2010**, *115*, D00H24. [CrossRef]
41. Hoareau, C.; Keckhut, P.; Noel, V.; Chepfer, H.; Baray, J.-L. A decadal cirrus clouds climatology from ground-based and spaceborne lidars above south of France (43.9° N–5.7° E). *Atmos. Chem. Phys. Discuss.* **2013**, *13*, 6379–6417. [CrossRef]
42. Keckhut, P.; Hauchecorne, A.; Bekki, S.; Colette, A.; David, C.; Jumelet, J. Indications of thin cirrus clouds in the stratosphere at mid-latitudes. *Atmos. Chem. Phys.* **2005**, *5*, 3407–3414. [CrossRef]
43. Keckhut, P.; Borchi, F.; Bekki, S.; Hauchecorne, A.; SiLaouina, M. Cirrus classification at mid-latitude from systematic lidar observations. *J. Appl. Meteorol. Clim.* **2006**, *45*, 249–258. [CrossRef]
44. Keckhut, P.; Perrin, J.-M.; Thuillier, G.; Hoareau, C.; Porteneuve, J.; Montouxc, N. Subgrid-scale cirrus observed by lidar at mid-latitude: Variability effects of the cloud optical depth. *J. Appl. Remote Sens.* **2013**, *7*, 073530. [CrossRef]
45. Montoux, N.; Keckhut, P.; Hauchecorne, A.; Jumelet, J.; Brogniez, H.; David, C. Isentropic modeling of a cirrus cloud event observed in the midlatitude upper troposphere and lower stratosphere. *J. Geophys. Res.* **2010**, *115*, D02202. [CrossRef]
46. Lamquin, N.; Stubenrauch, C.J.; Gierens, K.; Burkhardt, U.; Smit, H. A global climatology of upper-tropospheric ice supersaturation occurrence inferred from the Atmospheric Infrared Sounder calibrated by MOZAIC. *Atmos. Chem. Phys.* **2012**, *12*, 381–405. [CrossRef]
47. Voudouri, K.A.; Giannakaki, E.; Komppula, M.; Balis, D. Variability in cirrus cloud properties using a PollyXT Raman lidar over high and tropical latitudes. *Atmos. Chem. Phys.* **2020**, *20*, 4427–4444. [CrossRef]

48. Gouveia, D.A.; Barja, B.; Barbosa, H.M.J.; Seifert, P.; Baars, H.; Pauliquevis, T.; Artaxo, P. Optical and geometrical properties of cirrus clouds in Amazonia derived from 1 year of groundbased lidar measurements. *Atmos. Chem. Phys.* **2017**, *17*, 3619–3636. [CrossRef]
49. He, Q.S.; Li, C.C.; Ma, J.Z.; Wang, H.Q.; Shi, G.M.; Liang, Z.R.; Luan, Q.; Geng, F.H.; Zhou, X.W. The properties and formation of cirrus clouds over the Tibetan Plateau based on summertime lidar measurements. *J. Atmos. Sci.* **2013**, *70*, 901–915. [CrossRef]
50. Lakkis, S.G.; Lavorato, M.; Canziani, P.; Lacomi, H. Lidar observations of cirrus clouds in Buenos Aires. *J. Atmos. Sol.-Terr. Phy.* **2015**, *130–131*, 89–95. [CrossRef]
51. Nohra, R.; Parol, F.; Dubuisson, P. Comparison of Cirrus Cloud Characteristics as Estimated by A Micropulse Ground-Based Lidar and A Spaceborne Lidar CALIOP Datasets Over Lille, France (50.60 N, 3.14 E). *EPJ Web Conf.* **2016**, *119*, 16005. [CrossRef]
52. Seifert, P.; Ansmann, A.; Mu, D.; Wandinger, U.; Althausen, D.; Heymsfield, A.J. Cirrus optical properties observed with lidar, radiosonde, and satellite over the tropical Indian Ocean during the aerosol-polluted northeast and clean maritime southwest monsoon. *J. Geophys. Res.* **2007**, *112*, D17205. [CrossRef]
53. Yorks, J.E.; Hlavka, D.L.; Hart, W.D.; McGill, M.J. Statistics of cloud optical properties from airborne lidar measurements. *J. Atmos. Ocean. Tech.* **2011**, *28*, 869–883. [CrossRef]
54. Sherlock, V.; Garnier, A.; Hauchecorne, A.; Keckhut, P. Implementation and validation of a Raman lidar measurement of middle and upper tropospheric water vapour. *Appl. Opt.* **1999**, *38*, 5838–5850. [CrossRef]
55. Khaykin, S.; Godin-Beekmann, S.; Hauchecorne, A.; Pelon, J.; Ravetta, F.; Keckhut, P. Stratospheric smoke layer with unprecedentedly high backscatter observed by lidars above southern France. *Geophys. Res. Lett. Am. Geophys. Union* **2018**, *45*, 1639–1646. [CrossRef]
56. Bucholtz, A. Rayleigh-scattering calculations for the terrestrial atmosphere. *Appl. Opt.* **1995**, *34*, 2765–2773. [CrossRef]
57. Hoareau, C.; Keckhut, P.; Baray, J.-L.; Sarkissian, A.; Durry, G. Methodology for water monitoring in the upper troposphere with Raman lidar at Observatory of Haute-Provence. *J. Atmos. Ocean. Technol.* **2009**, *26*, 2149–2160. [CrossRef]
58. Lanzante, J.R. Resistant, robust and non-parametric techniques for the analysis of climate data: Theory and examples, including applications to historical radiosonde station data. *Int. J. Climatol.* **1996**, *16*, 1197–1226. [CrossRef]
59. Nellore, M.K.; Kannan, V.; Vellaisamy, A.L. A Statistical Method for Determining Optical and Geometrical Characteristics of Cirrus Clouds. *Climate* **2019**, *7*, 72. [CrossRef]
60. Li, Q.; Groß, S. Changes in cirrus cloud properties and occurrence over Europe during the COVID-19-caused air traffic reduction. *Atmos. Chem. Phys.* **2021**, *21*, 14573–14590. [CrossRef]
61. Córdoba-Jabonero, C.; Lopes, F.J.S.; Landulfo, E.; Cuevas, E.; Ochoa, H.; Gil-Ojeda, M. Diversity on subtropical and polar cirrus clouds properties as derived from both ground-based lidars and CALIPSO/CALIOP measurements. *Atmos. Res.* **2017**, *183*, 151–165. [CrossRef]
62. Gryspeerdt, E.; Quaas, J.; Goren, T.; Klocke, D.; Brueck, M. An automated cirrus classification. *Atmos. Chem. Phys.* **2018**, *18*, 6157–6169. [CrossRef]
63. Dekoutsidis, G.; Groß, S.; Wirth, M.; Krämer, M.; Rolf, C. Characteristics of supersaturation in midlatitude cirrus clouds and their adjacent cloud-free air. *Atmos. Chem. Phys.* **2023**, *23*, 3103–3117. [CrossRef]
64. Cadet, B.; Giraud, V.; Haeffelin, M.; Keckhut, P.; Rechou, A.; Baldy, S. improved re-trievals of the optical properties of cirrus clouds by a combination of lidar methods. *Appl. Opt.* **2005**, *44*, 1726–1734. [CrossRef] [PubMed]
65. Platt, C.M.R.; Dilley, A.C. Determination of the cirrus particle single-scattering phase function from lidar and solar radiometric data. *Appl. Opt.* **1984**, *23*, 380. [CrossRef]
66. Chen, W.N.; Chiang, C.W.; Nee, J.B. Lidar ratio and depolarization ratio for cirrus clouds. *Appl Opt.* **2002**, *41*, 6470–6476. [CrossRef] [PubMed]
67. Hersbach, H.; Bell, B.; Berrisford, P.; Biavati, G.; Horányi, A.; Muñoz Sabater, J.; Nicolas, J.; Peubey, C.; Radu, R.; Rozum, I.; et al. *ERA5 Hourly Data on Pressure Levels from 1940 to Present*; Copernicus Climate Change Service (C3S) Climate Data Store (CDS): Reading, UK, 2023. [CrossRef]
68. Chéruy, F.; Aires, F. Cluster Analysis of Cloud Properties over the Southern European Mediterranean Area in Observations and a Model. *Mon. Weather Rev.* **2009**, *137*, 3161–3176. [CrossRef]
69. Shcherbakov, V.; Gayet, J.F.; Jourdan, O.; Minikin, A.; Ström, J.; Petzold, A. Assessment of cirrus cloud optical and microphysical data reliability by applying statistical procedures. *J. Atmos. Ocean. Technol.* **2005**, *22*, 409–420. [CrossRef]
70. Jeggle, K.; Neubauer, D.; Lohmann, U. Identification of cirrus formation regimes using cluster analysis of back trajectories and satellite data. In Proceedings of the EGU General Assembly 2023, Vienna, Austria, 24–28 April 2023; p. EGU23-5002. [CrossRef]
71. Gordon, N.D.; Norris, J.R. Cluster analysis of midlatitude oceanic cloud regimes: Mean properties and temperature sensitivity. *Atmos. Chem. Phys.* **2010**, *10*, 6435–6459. [CrossRef]
72. Kurihana, T.; Moyer, E.J.; Foster, I.T. AICCA: AI-Driven Cloud Classification Atlas. *Remote Sens.* **2022**, *14*, 5690. [CrossRef]
73. Sassen, K.; Cho, B.Y. Subvisual-thin cirrus lidar dataset for satellite verification and climatological research. *J. Appl. Meteorol.* **1992**, *31*, 1275–1285. [CrossRef]
74. Mandija, F.; Sicard, M.; Comerón, A.; Alados-Arboledas, L.; Guerrero-Rascado, J.L.; Barragan, R.; Bravo-Aranda, J.A.; Granados-Muñoz, M.J.; Lyamani, H.; Porcar, C.M.; et al. Origin and pathways of the mineral dust transport to two Spanish EARLINET sites: Effect on the observed columnar and range-resolved dust optical properties. *Atmos. Res.* **2017**, *187*, 69–83. [CrossRef]

75. Mandija, F.; Chavez-Perez, V.M.; Nieto, R.; Sicard, M.; Danylevsky, V.; Añel, J.A.; Gimeno, L. The climatology of dust events over European continent using data of the Dust Regional Atmospheric Model. *Atmos. Res.* **2018**, *209*, 144–162. [CrossRef]
76. Reichardt, J. Optical and Geometrical Properties of Northern Mid-latitude Cirrus Clouds Observed with a UV Raman lidar. *Phys. Chem. Earth B* **1999**, *24*, 255–260. [CrossRef]
77. Sunilkumar, S.V.; Parameswaran, K. Temperature dependence of tropical cirrus properties and radiative effects. *J. Geophys. Res.* **2005**, *110*, D13205. [CrossRef]
78. Bankert, R.L.; SolBrig, J.E. Cluster Analysis of A-train data: Approximating the vertical cloud structure of oceanic cloud regimes. *J. Appl. Meteorol. Climatol.* **2015**, *54*, 996–1008. [CrossRef]
79. Li, Y.; Mahnke, C.; Rohs, S.; Bundke, U.; Spelten, N.; Dekoutsidis, G.; Groß, S.; Voigt, C.; Schumann, U.; Petzold, A.; et al. Upper-tropospheric slightly ice-subsaturated regions: Frequency of occurrence and statistical evidence for the appearance of contrail cirrus. *Atmos. Chem. Phys.* **2023**, *23*, 2251–2271. [CrossRef]
80. Schumann, U.; Poll, I.; Teoh, R.; Koelle, R.; Spinielli, E.; Molloy, J.; Koudis, G.S.; Baumann, R.; Bugliaro, L.; Stettler, M.; et al. Air traffic and contrail changes over Europe during COVID-19: A model study. *Atmos. Chem. Phys.* **2021**, *21*, 7429–7450. [CrossRef]
81. Schmidt, E. Die Entstehung von Eisnebel aus den Auspuffgasen von Flugmotoren. In *Deutschen Akademie der Luftfahrtforschung*; R. Oldenbourg: München, Germany, 1941; Volume 5, pp. 1–15.
82. Appleman, H. The formation of exhaust condensation trails by jet aircraft. *Bull. Am. Meteorol. Soc.* **1953**, *34*, 14–20. [CrossRef]
83. Dong, Z.; Ge, J.; Gao, A.; Zhu, Z.; Yan, J.; Mu, Q.; Su, J.; Yang, X.; Hu, X. Comparisons of cirrus clouds and their linkages to meteorology at the SACOL and the SGP sites. *Atmos. Res.* **2023**, *281*, 106467. [CrossRef]
84. Kaiser, H.F. The varimax criterion for analytic rotation in factor analysis. *Psychometrika* **1958**, *23*, 187–200. [CrossRef]
85. Li, Q.; Groß, S. Satellite observations of seasonality and long-term trends in cirrus cloud properties over Europe: Investigation of possible aviation impacts. *Atmos. Chem. Phys.* **2022**, *22*, 15963–15980. [CrossRef]
86. Horn, J.L. A rationale and test for the number of factors in factor analysis. *Psychometrika* **1965**, *30*, 179–185. [CrossRef] [PubMed]
87. Yeung, K.Y.; Ruzzo, W.L. *An Empirical Study on Principal Component Analysis for Clustering Gene Expression Data*; Technical Report; Department of Computer Science and Engineering, University of Washington: Seattle, WA, USA, 2000.
88. Wang, Z.; Sassen, K. Cirrus cloud microphysical property retrieval using lidar and radar measurements: II, Midlatitude cirrus microphysical and radiative properties. *J. Atmos. Sci.* **2002**, *59*, 2291–2302. [CrossRef]
89. Ge, J.; Zheng, C.; Xie, H.; Xin, Y.; Huang, J.; Fu, Q. Midlatitude cirrus cloudsat the SACOL site: Macrophysical prop-erties and large-scale atmosphericstates. *J. Geophys. Res. Atmos.* **2018**, *123*, 2256–2271. [CrossRef]
90. Pandit, A.K.; Gadhavi, H.S.; Venkat Ratnam, M.; Raghunath, K.; Rao, S.V.B.; Jayaraman, A. Long-term trend analysis and climatology of tropical cirrus clouds using 16 years of lidar data set over Southern India. *Atmos. Chem. Phys.* **2015**, *15*, 13833–13848. [CrossRef]
91. Ge, J.; Wang, Z.; Liu, Y.; Su, J.; Wang, C.; Dong, Z. Linkages between mid-latitude cirrus cloud properties and large-scale meteorology at the SACOL site. *Clim. Dyn.* **2019**, *53*, 5035–5046. [CrossRef]
92. Deng, M.; Mace, G.G. Cirrus microphysical properties and air motion statistics using cloud radar Doppler moments. Part II: Climatology. *J. Appl. Meteor. Climatol.* **2008**, *47*, 3221–3235. [CrossRef]
93. Sandhya, M.; Sridharan, S.; Indira Devi, M.; Niranjan, K.; Jayaraman, A. A case study of formation and maintenance of a lower stratospheric cirrus cloud over the tropics. *Ann. Geophys.* **2015**, *33*, 599–608. [CrossRef]